AER/AGS Open File Report 2026-01

Alberta Energy Regulator

Comprehensive Processing Workflow for Seismic Nodal Array Data: Application to the North Peace River Earthquake Sequence, Northwestern Alberta

AGS
ALBERTA GEOLOGICAL SURVEY

AER/AGS Open File Report 2026-01

Comprehensive Processing Workflow for Seismic Nodal Array Data: Application to the North Peace River Earthquake Sequence, Northwestern Alberta

H. Bui, J.A. Yusifbayov, M. Reyes Canales and C. Goerzen

Alberta Energy Regulator / Alberta Geological Survey

June 2026

ISBN 978-1-4601-5747-3

Bui, H., Yusifbayov, J.A., Reyes Canales, M. and Goerzen, C. (2026): Comprehensive processing workflow for seismic nodal array data: application to the North Peace River earthquake sequence, northwestern Alberta; Alberta Energy Regulator / Alberta Geological Survey, AER/AGS Open File Report 2026-01, 27 p.

Published June 2026 by:
Alberta Energy Regulator
Alberta Geological Survey
Suite 205
4999 – 98 Avenue NW
Edmonton, AB T6B 2X3
Canada

Tel: 780.638.4491
Email: AGS-Info@aer.ca
Website: ags.aer.ca

Contents

1 Introduction 1
2 Methodology 2
2.1 Seismic Nodes 2
2.2 Data Preprocessing 2
2.3 Event Detection and Classification 3
2.4 Seismic Phase Picking 4
2.5 Event Location 4
2.6 Local Magnitude Calculation and Catalogue Building 5
2.7 Source Mechanism Analysis 6
3 Application to the Seismic Nodal Array Data from the North Peace River Earthquake Sequence 7
3.1 Data Overview and Preprocessing 7
3.2 Event Detection and Seismic Phase Picking 10
3.3 Event Location 14
3.4 Local Magnitude Calculation and Catalogue Building 19
3.5 Source Mechanism Analysis 20
4 Discussion 20
5 Conclusions 22
6 References 22

Tables

Table 1. List of 12 events with local magnitude (M_L) ≥1.5 detected by the seismic nodal array during the three rounds of deployment (July 27 to November 15, 2023), Peace River region, northwestern Alberta. The table includes a comparison to the M_L of the same events detected by the regional array (Alberta Geological Survey, 2026). Abbreviations: dd, day; HH, hour; mm, month; MM, minute; SS, second; yyyy, year. 20

Figures

Figure 1. Map showing the locations of seven nodes (black triangles) overlaid on seismic event locations (orange circles) in the Peace River region (northwestern Alberta) recorded by the regional seismic array between January 2009 and February 2026 (Alberta Earthquake Dashboard; Alberta Geological Survey, 2026). 8
Figure 2. (a) A node deployed in the field. (b) Data harvested from nodes collected from the field. 8
Figure 3. Example of one day of raw three-component data recorded by a seismic node: (a) one day (24 hours) of waveform data; (b) zoomed in section of a raw data segment containing only noise; (c) zoomed-in section of a raw data segment containing one seismic event, with visible seismic phases, including a P-wave (P) arrival followed by an S-wave (S) arrival. The data include two horizontal components, h1 (in green) and h2 (in blue), and a vertical component, z (in red). Abbreviations: HH, hour; MM, minute; SS, second. 9
Figure 4. Example of various nonseismic signals and noise: (a) long and (b) short duration low-frequency nonseismic signals; (c) and (d) high-frequency nonseismic signals (spikes); (e) high-frequency nonseismic signal with a long duration. These signals are often random and have high amplitudes relative to the background noise, causing them to be incorrectly detected as potential events by an incoherent energy detector (short-time average / long-time average method). The data include two horizontal components, h1 (in green) and h2 (in blue), and a vertical component, z (in red). 9
Figure 5. An example of how the cutoff frequencies of a bandpass filter are determined. (a) Seismogram of a detrended event. (b) Seismogram of a detrended noise segment. (c) Amplitude spectrum

magnitude of the event and noise in linear format. (d) Amplitude spectrum magnitude of the event and noise in decibel (dB) format. The black rectangle in (c) shows the frequency range chosen for the bandpass filter. Abbreviations: f, frequency domain; Hz, hertz; t, time domain. 11
Figure 6. Seismograms of examples of excellent and probable events, and a noise record: (a) excellent event; (b) excellent event with a longer P-wave (P indicates arrival time) to S-wave (S indicates arrival time) travel-time distance; (c) probable event; (d) noise record. The data include two horizontal components, h1 (in green) and h2 (in blue), and a vertical component, z (in red). 12
Figure 7. Events identified from three rounds of data by using the short-time average / long-time average method. Between October 5 and October 12, 2023, no nodal array data were available due to a gap before the third deployment of nodes; consequently, no events were recorded during this time. 13
Figure 8. Examples of P-wave arrival picks (yellow dots) and S-wave arrival picks (black dots) on (a) a high-quality waveform and (b) a noisy waveform. The data include two horizontal components, h1 (in green) and h2 (in blue), and a vertical component, z (in red). 13
Figure 9. One-dimensional (1D) velocity model for the Peace River region, northwestern Alberta. Abbreviations: BLS, below land surface; V_P, P-wave velocity; V_S, S-wave velocity. 14
Figure 10. Comparison between seismic event locations obtained from the nodal array data and the locations of the same events (highlighted within the large filled green circle) detected by the regional seismic array (Alberta Geological Survey, 2026) in the Peace River region, northwestern Alberta, between July 27 and November 15, 2023: (a) map view; (b) and (c) depth views. All events were located using the Peace River one-dimensional velocity model (Bui et al., 2024). Abbreviation: BLS, below land surface. 16
Figure 11. (a) Map and (b) and (c) depth views of 340 seismic events detected and located using nodal array data (open blue circles; July 27 to November 15, 2023), plotted together with node locations (black triangles), nearby disposal wells (labelled with numbers), and background seismicity from the regional array (open gray circles; January 2009 to February 2026; Alberta Geological Survey, 2026) in the Peace River region, northwestern Alberta. Filled green circle indicates area with 26 events not detected by the regional array. Abbreviations: BLS, below land surface; M_L, local magnitude. 17
Figure 12. Estimated error in seismic event locations (error ellipsoids) in the Peace River region, northwestern Alberta, July 27 to November 15, 2023: (a) three-dimensional (3D) error ellipsoids; (b) map view; (c) and (d) depth views. Node locations and event locations are indicated by black triangles and blue circles, respectively. All coordinates are in UTM Zone 11N, NAD83. Abbreviation: BLS, below land surface. 18
Figure 13. Histogram of local magnitude estimates for seismic events recorded by the nodal array in the Peace River region, northwestern Alberta, between July 27 and November 15, 2023. Black squares represent the observed annual rate of exceedance for each magnitude bin, plotted on a logarithmic scale. The central blue line shows the Gutenberg-Richter (GR) parameters estimation, using the maximum likelihood method (Aki, 1965). The upper (red) and lower (green) curves show the uncertainty bounds of the GR parameters estimation. 19
Figure 14. Moment tensor inversion of selected seismic events (orange circles; see associated event numbers in Table 1 for further information) in the Peace River region, northwestern Alberta. All of the seismic event locations (blue circles) obtained from the nodal array data (July 27 to November 15, 2023) are also plotted on this map for reference. Major tectonic features (Peace River–Athabasca Arch and Buffalo High–Utikuma High domain boundary; Alberta Geological Survey, 2021) and lineaments (covering the Cretaceous to Precambrian interval; Mei, 2006) are also shown. 21

Acknowledgements

The authors would like to thank Jason Hendrick, Nick Roman, Shaurat Sayani, Alex MacNeil, Matt Grobe, Todd Shipman, Chris Filewich, Kelsey MacCormack, and Andrew Beaton (Alberta Geological Survey and Alberta Energy Regulator) for their constructive and helpful support developing this project.

Abstract

Seismic nodal arrays are increasingly used in local-scale seismic studies, offering a rapid, cost-effective deployment, and providing high-resolution event locations that can enhance understanding of seismic clusters. This report outlines a comprehensive processing workflow for seismic nodal array data, including preprocessing, event detection, phase picking, event location, magnitude estimation, catalogue building, and source mechanism analysis. Each step is described in detail and illustrated through a case study using three rounds of seismic nodal array data collected in the area north of the town of Peace River.

The results show that with just three months of deployment, the nodal array detected 340 events in the Peace River region, with the largest event in the catalogue having a local magnitude of 2.83. Among these, 29 events had local magnitudes greater than or equal to 1, and 13 of these events were not detected by the regional seismic array. Despite the limited spatial coverage with only seven seismic nodes, the event locations show good agreement with those recorded by the regional array. Most events occurred at depths between 4 and 6 km below the ground surface. Notably, the nodal array detected a small seismic cluster of 26 events within a 15 km radius of disposal wells that was not previously detected by the regional array. The North Peace River earthquake sequence is currently under assessment, and it is believed that the high-resolution catalogue from the nodal array data can help elucidate the potential induced seismic origin of this sequence.

1 Introduction

The spatial distribution and density of seismic stations play a critical role in the accuracy of earthquake detection, location, and source characterization. Dense and well-designed seismic networks are essential for improving the detectability of small-magnitude events and reducing uncertainties in event hypocentre locations. However, achieving optimal coverage is often challenging due to the high costs associated with equipment deployment and maintenance, as well as the frequency of seismic activity over a broad geographic extent.

The Alberta Geological Survey (AGS) has established a public seismic network known as the Regional Alberta Observatory for Earthquake Studies Network (RAVEN), with stations distributed across Alberta to monitor both natural earthquakes and induced seismicity related to industrial activities (Schultz and Stern, 2015). Over the years, the RAVEN network has expanded from eight real-time, continuously recording, three-channel broadband stations to a total of 36 stations, prioritizing areas with high seismic activities in the province. Seismic data from the RAVEN stations were further supplemented with the waveforms from private arrays deployed near industrial operations (Schultz et al., 2020). As of 2024, together with data shared by private operators, the AGS seismic monitoring system incorporates seismic waveforms from nearly 100 stations to monitor ongoing seismic activities across the province, including seismicity in the Fox Creek (Subsurface Order No. 2A [SSO2A]; Alberta Energy Regulator, 2024), Red Deer (Subsurface Order No. 7 [SSO7]; Alberta Energy Regulator, 2019), south of Grande Prairie, Peace River, Rocky Mountain House, and Redwater areas.

Regions such as Fox Creek and south of Grande Prairie (including the Kakwa, Musreau Lake, and Gold Creek areas) have benefited from relatively dense station coverage for some time, particularly since 2014, with the deployment of the RAVEN stations. This has allowed for more precise detection and characterization of seismic events over multiple studies (e.g., Schultz et al., 2015, 2017; Wang et al., 2016, 2020; Schultz and Wang, 2020; Yu et al., 2021; Li et al., 2022; Reyes Canales et al., 2022a, b). Other areas with emerging seismicity, such as the Peace River region, have only recently seen improvements in data coverage. Seismic activity in the Peace River area, particularly within the Reno seismic cluster, increased significantly in 2022 and 2023 following the November 2022 local magnitude (ML) 5.59 mainshock. Since then, improvements in data availability, driven by the Alberta Energy Regulator (AER) data mandate (How to Submit Seismic Waveform Data; Alberta Energy Regulator, 2025; Directive 065: Resources Applications for Oil and Gas Reservoirs; Alberta Energy Regulator, 2026) and data sharing from private operators, have enhanced monitoring capabilities. However, permanent station density in some areas of the Peace River region remains limited, particularly in other clusters in the Peace River region, peripheral to the Reno seismic cluster. Sparse seismic networks pose challenges for detecting small-magnitude events, accurately determining hypocentre locations, and resolving source mechanisms. For example, Wang et al. (2020) investigated a seismic cluster in Red Deer during 2019–2020 and demonstrated that limited station coverage contributed to significant discrepancies in event locations, hindering efforts to constrain source characteristics for potentially induced events.

To address the limitations of sparse station coverage, temporary nodal seismic arrays are increasingly used in local-scale studies (e.g., Hansen and Schmandt, 2015; Wang et al., 2020; Mesimeri et al., 2021; Sheng et al., 2021; Shearer et al., 2023). Nodal arrays offer rapid and cost-effective deployment, providing temporary station coverage suitable for recording aftershock sequences and investigating seismicity in regions with limited permanent stations. In Alberta, notable cases of using nodal arrays include deployments near the Red Deer (Wang et al., 2020) and Reno areas (Schultz et al., 2023; Li et al., 2024; Salvage et al., 2024; Gu et al., 2025; Reyes Canales et al., 2026). In the Red Deer case, Wang et al. (2020) successfully recorded over 400 events by installing a nodal array following the ML = 4.32 mainshock in March 2019, providing valuable insights into event distribution and potential source mechanisms. In the Reno case, the deployment of a nodal array following the ML = 5.59 mainshock in November 2022 provided high-resolution seismic event locations, with nearly 3300 events detected from three rounds of nodal array data, supporting investigations into the potential for an induced origin of the

seismicity (Li et al., 2024; Gu et al., 2025; Reyes Canales et al., 2026). These cases demonstrate the growing importance of nodal arrays in enhancing the quality and resolution of local seismic monitoring to investigate emerging cases of induced seismicity. Both studies used a rapid-response method by deploying seismic nodes to record aftershocks. This approach enabled improved detection of smaller-magnitude events, enhanced data quality, and more accurate local magnitude estimations due to the proximity of the instruments. As a result, the nodal array data contributed to more complete seismic catalogues, enhanced the resolution of event distributions, better characterized source mechanisms and faulting, and supported a better understanding of the spatiotemporal evolution of regional seismic activity and its relationship with anthropogenic activity.

Alongside the deployed network array and its rapid installation, a robust data processing workflow is a critical factor to obtaining high-quality results. Nodal arrays often record large volumes of continuous waveform data, resulting in datasets that can reach hundreds of gigabytes. Efficient and detailed workflow is therefore necessary for noise attenuation, event detection and location, and magnitude estimation. Proper filtering, consistent parameter tuning, and reproducible processing steps are critical for enhancing signal-to-noise ratios, preserving waveform amplitude and polarity, and accurately characterizing seismic event location and magnitude (Wang et al., 2020; Li et al., 2024; Gu et al., 2025).

At the AGS, a comprehensive processing workflow has been developed specifically for seismic nodal array data. The focus of this report is to outline the main steps of the workflow, including data preprocessing, event detection, event location, seismic catalogue building, and source mechanism analysis. The North Peace River seismic nodal array is used as a case study for high-resolution, local seismic monitoring. From the RAVEN network, three active seismic clusters have been identified in the Peace River region: North Peace River, North Heart, and Reno. Events in the North Heart and Reno seismic clusters are considered induced seismicity associated with nearby disposal activities (Reyes Canales et al., 2026), whereas events in the North Peace River seismic cluster are currently under assessment as their origins are still being evaluated. To enhance data coverage in this area and support investigations into the origin of this cluster, a temporary array of seven three-component (3C; 5 hertz [Hz]) Fairfield ZLand nodal geophones (Ringler et al., 2018) were deployed. The array recorded continuous waveform data during three deployments between July 27 and November 15, 2023, at a sampling rate of 250 Hz. The following sections include a description of the detailed processing steps and demonstrate how the processing workflow was applied to the nodal array dataset collected from the north of the town of Peace River. Investigations to determine the origin of the North Peace River earthquake sequence are beyond the focus of this report, and they are to be undertaken in further studies.

2 Methodology

2.1 Seismic Nodes

Fairfield ZLand nodes are fully sealed, portable, all-in-one 3C seismic instruments with each node containing the battery, sensor, electronics, timing circuitry, and memory necessary for recording and storing continuous seismic data for up to approximately 30 days (Berg, 2022). These 3C nodal geophones are sensitive to frequencies above 0.1 Hz while maintaining a relatively stable sensitivity at higher frequencies (Ringler et al., 2018; Gu et al., 2025). Their compact, lightweight design enables a rapid and cost-effective deployment, which has led to an increase in their use by both industry and academia for analyzing local seismicity, aseismic sources, and anthropogenic noise (Hansen and Schmandt, 2015; Gu et al., 2025).

2.2 Data Preprocessing

Preprocessing of nodal data is a critical step that facilitates subsequent analysis. It typically includes data conversion, data detrending, and noise filtering.

First, raw waveform data are retrieved from the nodes after field collection for preprocessing. The extracted seismic data are initially in a Fairfield custom file format (.fcnt). To facilitate further processing, the data are converted from .fcnt format to a more widely used miniSEED (.mseed) format. Daily recordings contain three components, two horizontal and one vertical, along with metadata in the file header. The metadata includes information such as recording time and date, station network and location, sampling rate, and the number of data samples.

The next step is data detrending, which involves removing linear trends from the time-series data. Usually, raw seismic data recorded at the stations are not centred on the x-axis. The mean value of the data is thus subtracted from the original time-series data to centre the signal around the x-axis before further analysis.

Finally, noise filtering is applied to suppress unwanted noise and improve the signal-to-noise ratio (SNR). Event detection algorithms generally perform more effectively on preconditioned data, as signal conditioning and enhancement filters can significantly improve data quality (Maxwell, 2014; Bui and van der Baan, 2020). The most common conditioning approach involves frequency-domain filters such as highpass, bandpass, or lowpass filters (Maxwell, 2014). However, the preferred option is to minimize the involvement of filters to preserve the signals (Maxwell, 2014). In this study, a bandpass filter was applied to attenuate noise outside of the target frequency range while preserving seismic signals. To determine the optimal corner frequencies for a bandpass filter, amplitude spectrum analysis is performed on both the detrended seismic signals and background noise. Seismic events and background noise often differ in character and frequency content, allowing the determination of the dominant frequency range of the events and selection of appropriate cutoff frequencies based on the amplitude spectrum. Once the corner frequencies are obtained, the bandpass filter is applied to the data from each station to enhance the data quality.

2.3 Event Detection and Classification

The short-time average / long-time average (STA/LTA) method is a straightforward technique for detecting seismic events and weak motions in seismology (Trnkoczy, 1999; Eaton, 2018). This method requires little to no information on the signals to be detected. This algorithm involves the use of two consecutive moving windows, an STA window and an LTA window. It continuously computes the average values of the absolute amplitude or energy of the signal in these two windows and then computes the ratio between them (Trnkoczy, 1999). The STA window is sensitive to a sudden increase in amplitude or energy (often the result of seismic events) whereas the LTA window represents the average amplitude of the background noise (Trnkoczy,1999; Oye and Roth, 2003).

In the STA/LTA method, the generalized expressions for the STA and LTA windows (Akram and Eaton, 2016) for data sample i of time series s(t) are given by

$$STA_i(s) = \frac{1}{N_S}\sum_{j=1}^{i+N_S-1} CF_j(s), \quad (1)$$

$$LTA_i(s) = \frac{1}{N_L}\sum_{j=1-N_L+1}^{i+N_S-1} CF_j(s), \quad (2)$$

characteristic function (CF) providing a measure of signal amplitude within a time window $s(t)$, which is the data in the STA and LTA windows. There are different choices for the CF function. In this study, Allen's (1978) characteristic function $CF_A(t)$ was used and is defined as

$$CF_A(t) = f(t)^2 + \alpha f'(t)^2, \quad (3)$$

where $f(t)$ is the time series (seismic trace) with the first difference $f'(t)$ and α is a weighting constant, which is usually set at 3. This CF function $CF_A(t)$ was designed to enhance the changes in both amplitude and frequency content of the seismic trace, and it can be easy to compute. This CF function was used in the STA/LTA algorithm as the arrival phase in the seismic time series is indicated by a change in the frequency content or the amplitude of both parameters.

As well, to avoid keeping long data vectors in the memory and reduce the computation time effectively for the STA/LTA algorithm, the recursive equation from Withers et al. (1998) was used. The STA and LTA are then calculated as

$$STA_i = C_1 x_i + (1 - C_1) STA_{i-1}, \quad (4)$$

and

$$LTA_i = C_2 x_i + (1 - C_2) LTA_{i-1}, \quad (5)$$

where $C_1 = 1/w_s$ and $C_2 = 1/w_l$; w_s, w_l are the STA and LTA window lengths, respectively; x_i is the time series with the time index i. After obtaining the STA and LTA values using Equations 4 and 5, the value of the STA/LTA ratio for the sample i was then given by

$$\left(\frac{STA}{LTA}\right)_i (N_S, N_L) = \frac{STA_i}{LTA_i}. \quad (6)$$

When the STA/LTA ratio is higher than a user-defined threshold, a potential event is triggered and extracted from the data. After that, the detection outcomes were inspected and each detected event was classified, which is often subjective, depending on the processing purposes. The detection process can result in one of four possible outcomes: true positive, false positive, true negative, or false negative. A true positive (true event) occurs when an event is correctly identified, whereas a false positive (false trigger/false alarm) is when noise is incorrectly detected as a potential event. A true negative occurs when an event does not happen and is correctly attributed as such. A false negative (missed event) occurs when an event occurs, but the detector fails to recognize it as a potential event.

2.4 Seismic Phase Picking

After the event classification step, P- and S-wave arrival times were picked, as it is crucial for precise event location. Seismograms contain different types of seismic phases, including body waves and surface waves (Bormann et al., 2012). Body waves include compressional P-waves (longitudinal waves) and shear S-waves (transverse waves) that both propagate through the Earth's interior. These waves are strongly affected by refraction, reflection, and mode conversion at major boundaries (e.g., the Mohorovičić [Moho] discontinuity), which separate geological layers with significant contrasts in density and velocity (Bormann et al., 2012). Surface waves, in contrast, travel near the Earth's surface and typically exhibit lower frequencies and larger amplitudes than body waves (Bormann et al., 2012).

The P-wave onsets are often difficult to pick due to their weak amplitudes, whereas S-waves are generally easier to identify due to their stronger energy and larger amplitudes. Typically, the P-wave and S-wave phases are manually picked on the vertical component and one of the horizontal components of the seismogram, respectively. This can be time consuming, especially when handling large datasets. One way to accelerate this step is to employ a semiautomatic picking method. This approach combines cross-correlation techniques with the Akaike information criterion (AIC) to detect P- and S-wave onsets (Sleeman and Van Eck, 1999).

2.5 Event Location

Accurate event locations provide insights into the spatial distribution of events and contribute to a better understanding of the origin of seismic clusters. The earthquake location is a nonlinear problem with four unknowns, including three spatial coordinates of the hypocentre and the event origin time, which is the occurrence time of the initial energy release of a seismic event (Lomax et al., 2009). Usually, the locations are determined using arrival times at recording stations. In a nonhomogeneous medium, the observed arrival time, t_{obs}, of an event at a given station is related to its hypocentral location through

$$t_{obs} = t_0 + \int_{r_0(s)} u(r_0) ds, \quad (7)$$

where t_0 is the event origin time, $r_0(s)$ is a point at source-receiver distance s along the ray path r_0, and u is the slowness ($u = 1/v$, where v is the velocity of the seismic waves propagating in the medium; Lomax et al., 2009). In a homogeneous velocity field, the predicted travel time, t_{pred}, is a function of the receiver coordinates (x_R, y_R, and z_R), coordinates of an assumed hypocentre (x_a, y_a, and z_a), and velocity (v) and is given as

$$t_{pred} = \frac{\sqrt{(x_R - x_a)^2 + (y_R - y_a)^2 + (z_R - z_a)^2}}{v}. \quad (8)$$

In a nonhomogeneous velocity field, the predicted travel times are typically obtained using ray tracing. With four unknowns, estimating the event location can be described as an inverse problem. At least four arrival time observations are needed to determine the spatial coordinates of the hypocentre and the origin time (Waldhauser and Ellsworth, 2000; Havskov and Ottemoller, 2010). A solution is generally sought that minimizes the sum of the differences between the observed and predicted arrival times.

The accuracy of the estimated locations depends on various factors, such as data quality, phase picking, velocity model, acquisition geometry, and location algorithms (Pavlis, 1986; Wuestefeld et al., 2018). Poor data quality often leads to errors in phase picking, negatively affecting the event location (Eisner et al., 2009, 2010; Cipolla et al., 2011; Maxwell, 2014; Castellanos and van der Baan, 2015). Limited sensor azimuthal coverage can also cause potential biases in the estimated hypocentres (Eisner et al., 2009, 2010; Maxwell, 2014). Uncertainties in the velocity model can also introduce errors in the estimated hypocentres (Pavlis, 1986), since the subsurface is often an anisotropic medium with significant differences in vertical and horizontal velocities due to lithology, layering, and rock fabric (Tsvankin et al., 2010; Cipolla et al., 2011). Location algorithms using different optimization methods can also result in differences in the resolved locations (Pavlis, 1986; Wuestefeld et al., 2018).

The grid search method is widely employed due to its simplicity; however, it is computationally prohibitive when locating events over a large search space with small grid spacing (Lomax et al., 2000; Bui and van der Baan, 2024). Different approaches are proposed for resolving this limitation. Lomax et al. (2000, 2009) and Lomax and Curtis (2001) employ importance sampling methods, including Metropolis-Gibbs and oct-tree, to resolve the inefficient, exhaustive grid searches. See Bui and van der Baan (2024) for more details.

Lomax et al. (2000) and Lomax and Curtis (2001) conclude that the Metropolis-Gibbs and oct-tree methods are substantially faster than a pure grid search, with the oct-tree method being simpler, faster, more stable, and more complete than the Metropolis-Gibbs approach. Thus, in this study, the oct-tree search method developed by Lomax et al. (2000) was used within the NonLinLoc software package (Lomax et al., 2000, 2014) to determine event locations.

2.6 Local Magnitude Calculation and Catalogue Building

Local magnitude (M_L) is the most widely reported magnitude scale in earthquake catalogues and can be written as

$$M_L = \log(A) - \log(A_0) + S, \quad (9)$$

where A is half of the peak-to-peak amplitude (mm) measured on a horizontal component of the ground motion data, $-\log(A_0)$ is the regional distance correction term, and S is a station correction term, which accounts for any systematic amplitude difference (Gutenberg and Richter, 1956; Boore, 1989; Yenier, 2017).

Proper correction of observed amplitudes for regional attenuation and site effects is essential for accurate magnitude estimation. In this study, a regionally calibrated M_L equation developed by Yenier (2017) for the Western Canada Sedimentary Basin (WCSB) was used; it accounts for regional attenuation characteristics. This equation is based on a well-constrained, empirically derived model that utilizes a rich ground-motion dataset from both local and regional seismic networks in Alberta.

Through assessment of amplitude decay with distance, Yenier (2017) found that interference between direct waves and postcritical Moho reflections modifies the attenuation pattern within the 100–200 km distance range. To account for these attenuation effects, the distance correction term $-\log(A_0)$ for earthquakes in the WCSB is parameterized using a trilinear function:

$$-\log A_0 = \begin{cases} 1.399\log(R) + 0.001R + 0.102 & R \leq 100\ km \\ -0.727\log(R) + 0.001R + 4.354 & 100\ km\ < R \leq 220\ km \\ 1.806\log(R) + 0.001R - 1.579 & R > 220\ km \end{cases}, \quad (10)$$

where R is the hypocentral distance in kilometres.

After calculating event local magnitudes, the final step is catalogue building. The main elements of an earthquake catalogue include event date and time, hypocentre location (latitude, longitude, and depth), and local magnitude. Additional information, such as the number of P- and S-wave phase observations used in the location process and moment magnitude, can be included if available. The earthquake catalogue can then be used for further analyses and interpretation, such as analyses of trends and frequencies of seismic events over time or performing moment tensor inversion, to support a better understanding of earthquake sequences and emerging seismic clusters.

2.7 Source Mechanism Analysis

After building the earthquake catalogue, one of the further processing steps that can contribute to a better understanding of earthquake source characteristics is moment tensor inversion. The resulting moment tensor depends on the fault orientation and source strength and characterizes the earthquake source (Stein and Wysession, 2009). Bui et al. (2024) provided a detailed case study of moment tensor inversion analysis applied to an M_L = 3.7 seismic event in central Alberta.

There are three primary techniques for moment-tensor inversion: the first-motion polarity method, amplitude methods (including amplitude-based and S/P amplitude–ratio approaches), and the full-waveform method (Eyre and van der Baan, 2015; Bui et al., 2024). Among these, amplitude methods provide better constraints than the first-motion polarity method and are relatively simple compared to the full-waveform method (Hardebeck and Shearer, 2003; Eyre and van der Baan, 2015). These methods incorporate a larger number of observations than first-motion polarity techniques. Furthermore, unlike the binary nature of polarity data (upwards or downwards), amplitude data have a range of values, resulting in a better-constrained orientation of the P- and S-wave radiation (Hardebeck and Shearer, 2003). For these reasons, an amplitude-based method that utilizes both P- and S-wave amplitudes was used to compute the moment tensors of seismic events.

The seismic-wave amplitudes recorded at the receivers are the result of the source mechanism (approximated by the moment tensor) convolved with the propagation effects (e.g., Green's functions) and instrument response (Eyre and van der Baan, 2017). The moment-tensor inversion algorithm calculates Green's functions using the equations for particle motion generated by the P- and S-wave radiations from a point source in a homogeneous elastic medium (Aki and Richards, 2002). The P- and S-wave amplitudes recorded on a given receiver at position x and time t are given as

$$a_i^P(x,t) = \frac{1}{4\pi r\rho\alpha^3}\{\gamma_i\gamma_j\gamma_k M_{jk}\}, \quad (11)$$

$$a_i^S(x,t) = \frac{1}{4\pi r\rho\beta^3}\{(\delta_{ij} - \gamma_i\gamma_j)\gamma_k M_{jk}\}, \quad (12)$$

where i, j, k = x, y, z; r is the source-receiver distance (m); ρ is the density (kg/m^3); α and β are the P- and S-wave velocities (m/s), respectively, obtained from the previous step; $\gamma_i, \gamma_j, \gamma_k$ are the directions cosine from the source to the receiver; M is the moment tensor; and δ_{ij} is the Kronecker delta (Aki and Richards, 2002; Eyre and van der Baan, 2017). The amplitudes in Equations 11 and 12 can be rewritten in a matrix form:

$$\begin{bmatrix} d_1 \\ d_2 \\ \vdots \\ d_n \end{bmatrix} = \begin{bmatrix} G_{11} & G_{12} & G_{13} & G_{14} & G_{15} & G_{16} \\ \vdots & \vdots & \vdots & \vdots & \vdots & \vdots \\ \vdots & \vdots & \vdots & \vdots & \vdots & \vdots \\ G_{n1} & G_{n2} & G_{n3} & G_{n4} & G_{n5} & G_{n6} \end{bmatrix} \begin{bmatrix} m_1 \\ m_2 \\ \vdots \\ m_6 \end{bmatrix}, \quad (13)$$

where d_i are the observed ground displacement amplitudes at different arrival times at receiver i (i = 1: n, n is the number of receivers); G is an n by 6 matrix containing the Green's functions (synthetic amplitudes of ground motion displacements) calculated using an appropriate velocity model; and m_i are the six elements, M_{11}, M_{22}, M_{33}, M_{12}, M_{13}, and M_{23} of the moment tensor (Forouhideh and Eaton, 2009). The least squares method was then used to find an approximate solution to the system of n linear equations (Equation 13). The solution (Eyre and van der Baan, 2017) can be given as

$$m = (G^T G)^{-1} G^T d, \quad (14)$$

where T indicates a matrix transpose, provided $(G^T G)^{-1}$ exists (i.e., provided G has full column rank). This equation finds an approximate solution when no exact solution exists, and it gives an exact solution when one does exist.

3 Application to the Seismic Nodal Array Data from the North Peace River Earthquake Sequence

3.1 Data Overview and Preprocessing

The Peace River region has three main active seismic clusters (Figure 1). Seismic events in the North Heart and Reno clusters have been recorded since 2016 and 2017, respectively, and are considered to be induced earthquakes, primarily associated with water disposal activities (Schultz et al., 2023; Salvage et al., 2024; Reyes Canales et al., 2026). In contrast, the first event in the AGS catalogue recorded in the North Peace River cluster dates back to 2009 (Alberta Earthquake Dashboard; Alberta Geological Survey, 2026), and the cluster remains under assessment while its origin (natural or induced) is still being determined. To improve seismic coverage and support investigations into the causes of this cluster, the AGS deployed a temporary array of seven 3C nodal geophones. The deployment occurred in three rounds between July 27 and November 15, 2023, with an average lifespan of 30 days per round.

Figure 1 shows the locations of the nodes plotted with background seismicity recorded by the regional seismic array between January 2009 and February 2026. Nodes 3–7 were deployed around the cluster, whereas nodes 1 and 2 were positioned farther away to detect potential seismicity between the North Peace River cluster and the Reno and North Heart clusters. Figure 2a shows the field deployment of a node being oriented towards the true geographic north using a compass and carefully levelled, to prolong the battery level of the nodes. After acquiring a reliable Global Positioning System signal, the node was buried underground to record seismic data. Figure 2b illustrates the data harvest process at the AGS Mineral Core Research Facility in Edmonton. Approximately 200 gigabytes of raw seismic 3C data (with a sampling rate of 250 Hz) were collected and used for processing. An example of one full day's worth of raw 3C data is displayed in Figure 3a. Figure 3b highlights a portion of the data in Figure 3a that contains only noise, whereas Figure 3c displays a data segment that includes a seismic event with clear P- and S-wave arrivals.

Relatively high-quality data were obtained from the seismic nodal array. However, since the nodes continuously record signals, they capture not only seismic events but also various nonseismic signals and different types of high-amplitude random noise. Figure 4 shows examples of nonseismic signals present in the data. These signals are likely a consequence of the shallow deployment depth of the nodes, approximately 0.3 m below the surface, which made the nodes susceptible to ambient noise. These noise sources may include human traffic, agricultural activities, industrial operations, mining activities, and wind.

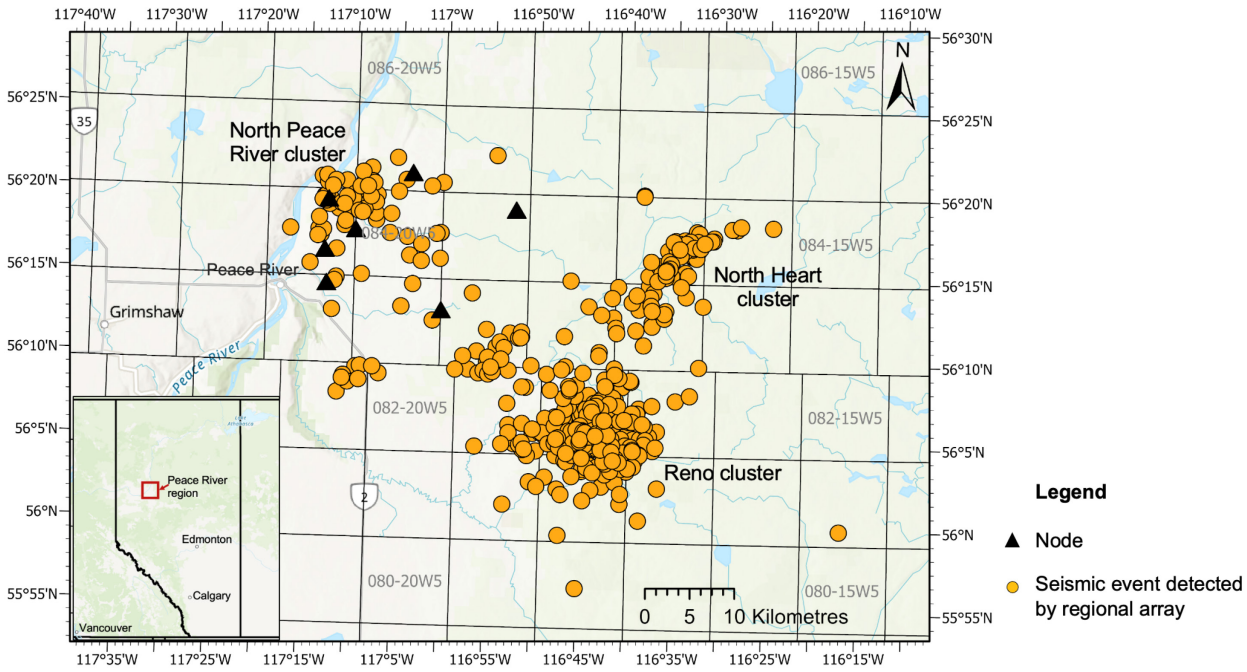

Figure 1. Map showing the locations of seven nodes (black triangles) overlaid on seismic event locations (orange circles) in the Peace River region (northwestern Alberta) recorded by the regional seismic array between January 2009 and February 2026 (Alberta Earthquake Dashboard; Alberta Geological Survey, 2026).

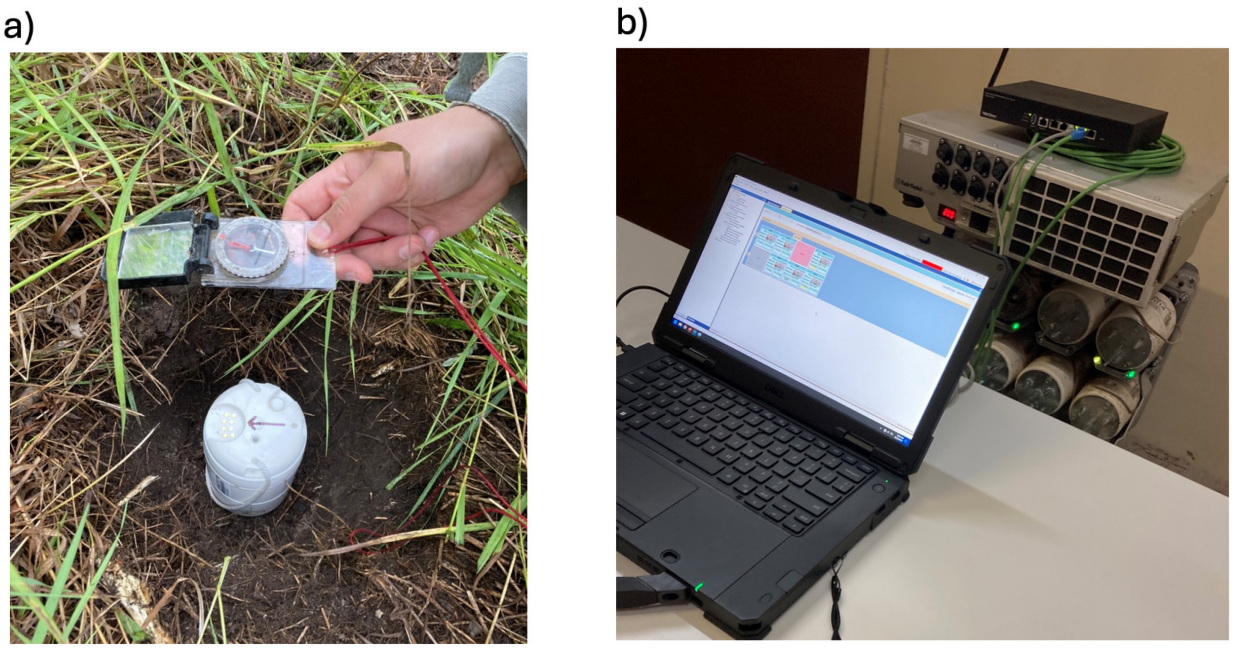

Figure 2. (a) A node deployed in the field. (b) Data harvested from nodes collected from the field.

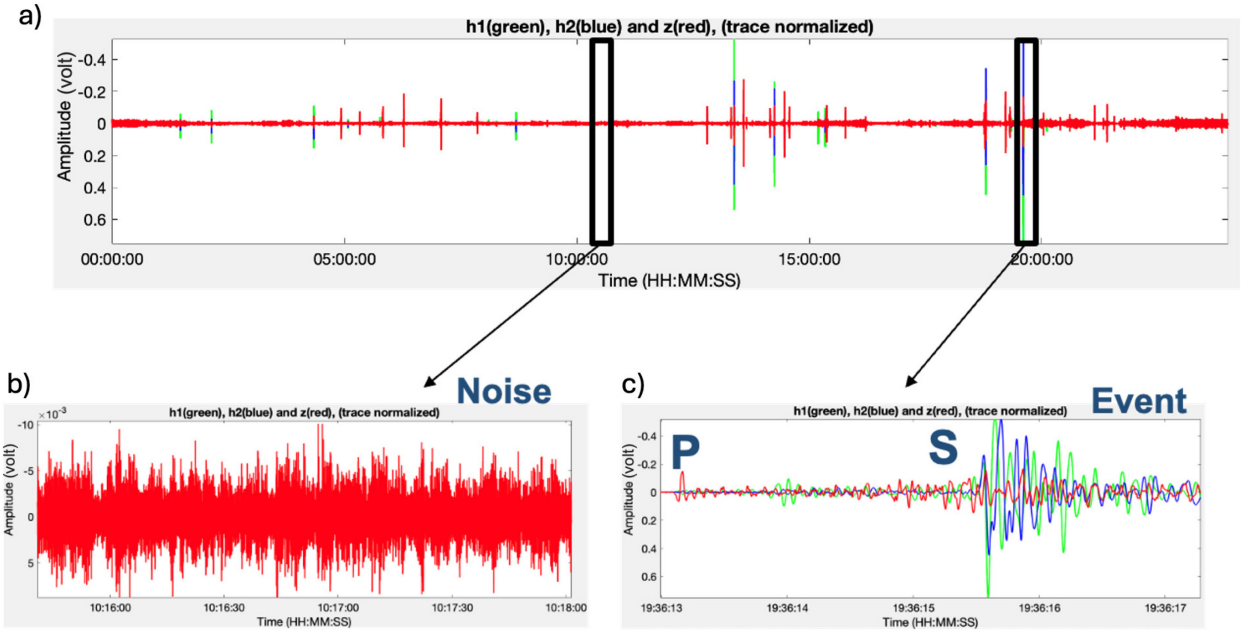

Figure 3. Example of one day of raw three-component data recorded by a seismic node: (a) one day (24 hours) of waveform data; (b) zoomed in section of a raw data segment containing only noise; (c) zoomed-in section of a raw data segment containing one seismic event, with visible seismic phases, including a P-wave (P) arrival followed by an S-wave (S) arrival. The data include two horizontal components, h1 (in green) and h2 (in blue), and a vertical component, z (in red). Abbreviations: HH, hour; MM, minute; SS, second.

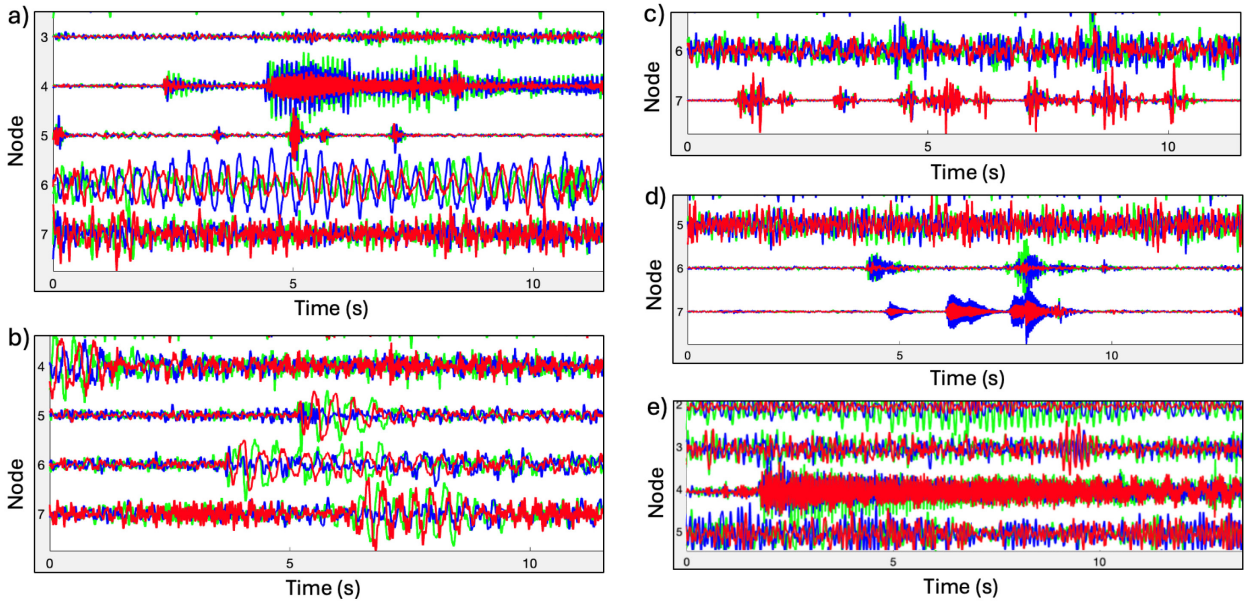

Figure 4. Example of various nonseismic signals and noise: (a) long and (b) short duration low-frequency nonseismic signals; (c) and (d) high-frequency nonseismic signals (spikes); (e) high-frequency nonseismic signal with a long duration. These signals are often random and have high amplitudes relative to the background noise, causing them to be incorrectly detected as potential events by an incoherent energy detector (short-time average / long-time average method). The data include two horizontal components, h1 (in green) and h2 (in blue), and a vertical component, z (in red).

After the data were harvested from the field centre, the preprocessing steps were performed, including conversion of the data from .fcnt to .mseed format, signal detrending, and noise attenuation. The .fcnt format is the original data format extracted from the nodes after being collected from the field. The data were converted to the more widely used .mseed format to facilitate further processing. To read the .fcnt data files, the Python module obspy.io.rg16 - Receiver Gather v1.6 read support for ObsPy (see https://docs.obspy.org/packages/obspy.io.rg16.html for more details) was used and then the data were written and saved along with the metadata in .mseed files. The obspy.io.rg16 module provides functions to read waveform data from the Receiver Gather 1.6-1 format, which is used to store continuous data recorded by Fairfield ZLand nodes.

Next, signal detrending was performed and a bandpass filter was applied to suppress noise in the data. The optimal cutoff frequencies for the bandpass filter were determined through spectral analysis. Figure 5a and Figure 5b shows the seismograms of a raw seismic event and noise, respectively, with their corresponding amplitude spectrum magnitude plots shown in Figure 5c and d in linear and decibel (dB) formats. The amplitude spectrum plots indicate that the dominant frequency of the seismic signal ranges from 3 to 30 Hz, with a peak frequency of around 7–15 Hz. Based on this spectral analysis, a soft bandpass filter was designed with corner frequencies of 1 and 40 Hz (highlighted by the black rectangle in Figure 5c) to attenuate noise prior to event detection.

3.2 Event Detection and Seismic Phase Picking

After preprocessing, the STA/LTA method was applied to detect and extract potential seismic events from the preconditioned data. For the parameter setting, the STA window length was set to three times the dominant period of the signal, and the LTA window length was set to five times longer than the STA window. Based on spectral analysis of representative signals, the dominant period was approximately 0.07 s; therefore, the STA and LTA windows were set to 0.2 s and 1.0 s, respectively. A potential event is triggered and extracted when the STA/LTA ratio exceeds a detection threshold and the signal is observed by at least three nodes, with visible P- and S-wave arrivals. Potential events with a window length of 15 s were extracted to ensure both P- and S-wave phases were included.

A relatively low STA/LTA detection threshold of 2 was used to increase sensitivity and capture ‘almost’ events, including weak or noisy events. The detected events were then classified into three categories: excellent events, probable events, and noise records. Figure 6 shows examples of multiple excellent events, one probable event, and a noise record. Excellent events (Figure 6a and Figure 6b) are those having pickable P- and S-wave phases. These events were included in the final event detection results and used for subsequent event location. Probable events (Figure 6c) are likely seismic events but are often noisy and it is difficult to pick either P- or S-wave phases, making them inadequate for accurate event location. Noise records (Figure 6d) are false positives caused by high-amplitude, nonseismic signals. Since the STA/LTA method is an incoherent energy detector, using a low threshold increases the number of false alarms significantly, making the event classification process time consuming.

After the event detection and manual classification step, a total of 340 true excellent events were identified and extracted. Among these, 29 events had local magnitudes greater than or equal to 1, and 13 of these events were not detected by the regional seismic array. Figure 7 shows the event detection results from the three rounds of seismic nodal array data collection. Nearly every day included recoded seismic events, with the highest daily count being 16 events on August 8, 2023. There was a period between October 5 and 12, 2023, with no nodal array data due to a gap before the third deployment of nodes; consequently, no events were recorded during this period.

After that, the P- and S-wave arrival times were manually picked for all 340 events. Given that the dataset consists of just over 300 events recorded by only seven nodes, manual picking was appropriate to ensure accurate phase arrival times. While many events exhibited high-quality waveforms, others were relatively noisy, making phase picking more difficult. Figure 8a shows an example of a high-quality event with strong P- and S-wave arrivals. In contrast, Figure 8b shows a noisy waveform, with only three nodes (4,

5, 6) showing both P- and S-wave arrivals. The signal is very noisy at node 6. Although the P- and S-wave arrivals are distinguishable, accurate picking is challenging in this case.

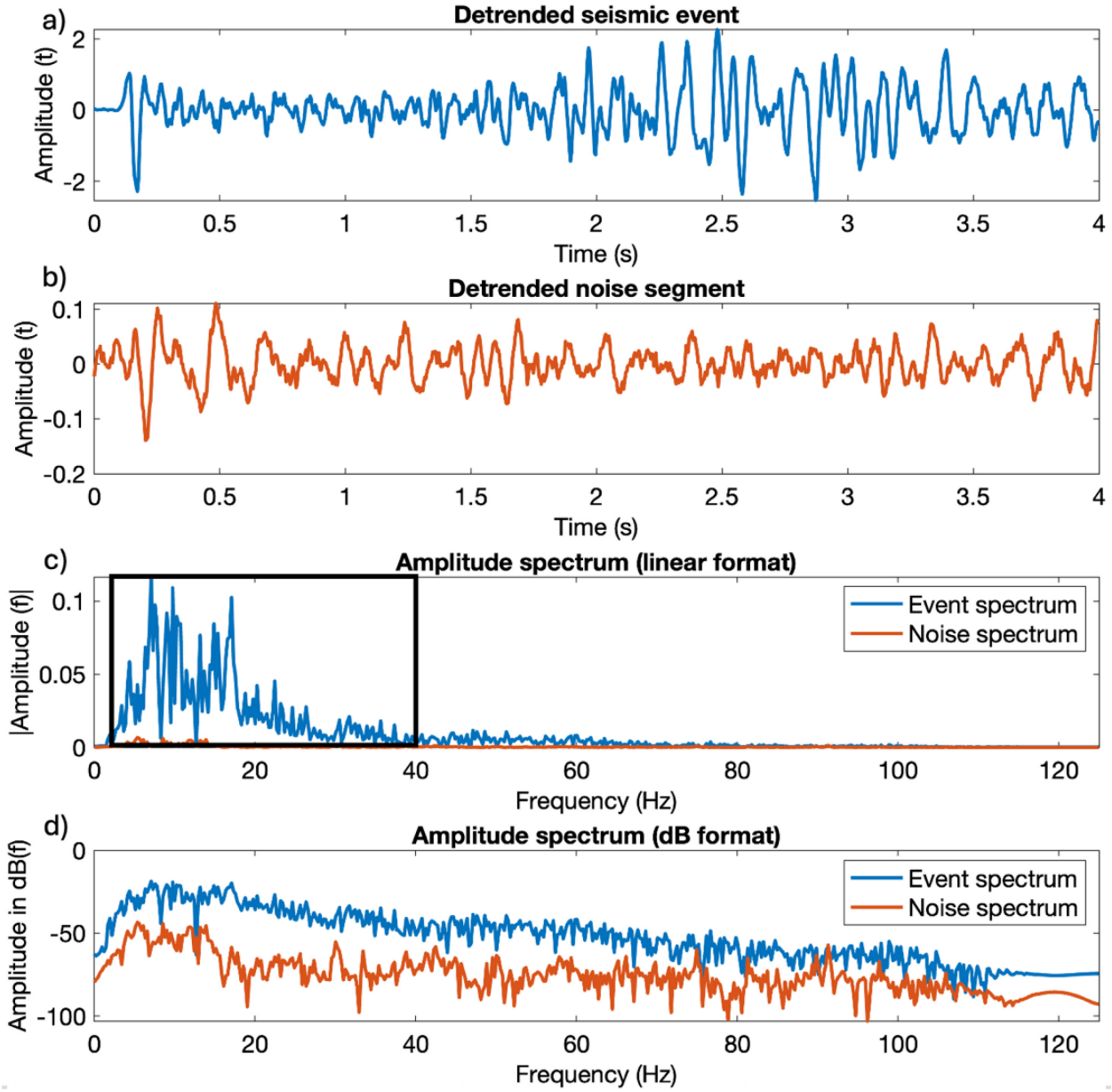

Figure 5. An example of how the cutoff frequencies of a bandpass filter are determined. (a) Seismogram of a detrended event. (b) Seismogram of a detrended noise segment. (c) Amplitude spectrum magnitude of the event and noise in linear format. (d) Amplitude spectrum magnitude of the event and noise in decibel (dB) format. The black rectangle in (c) shows the frequency range chosen for the bandpass filter. Abbreviations: f, frequency domain; Hz, hertz; t, time domain.

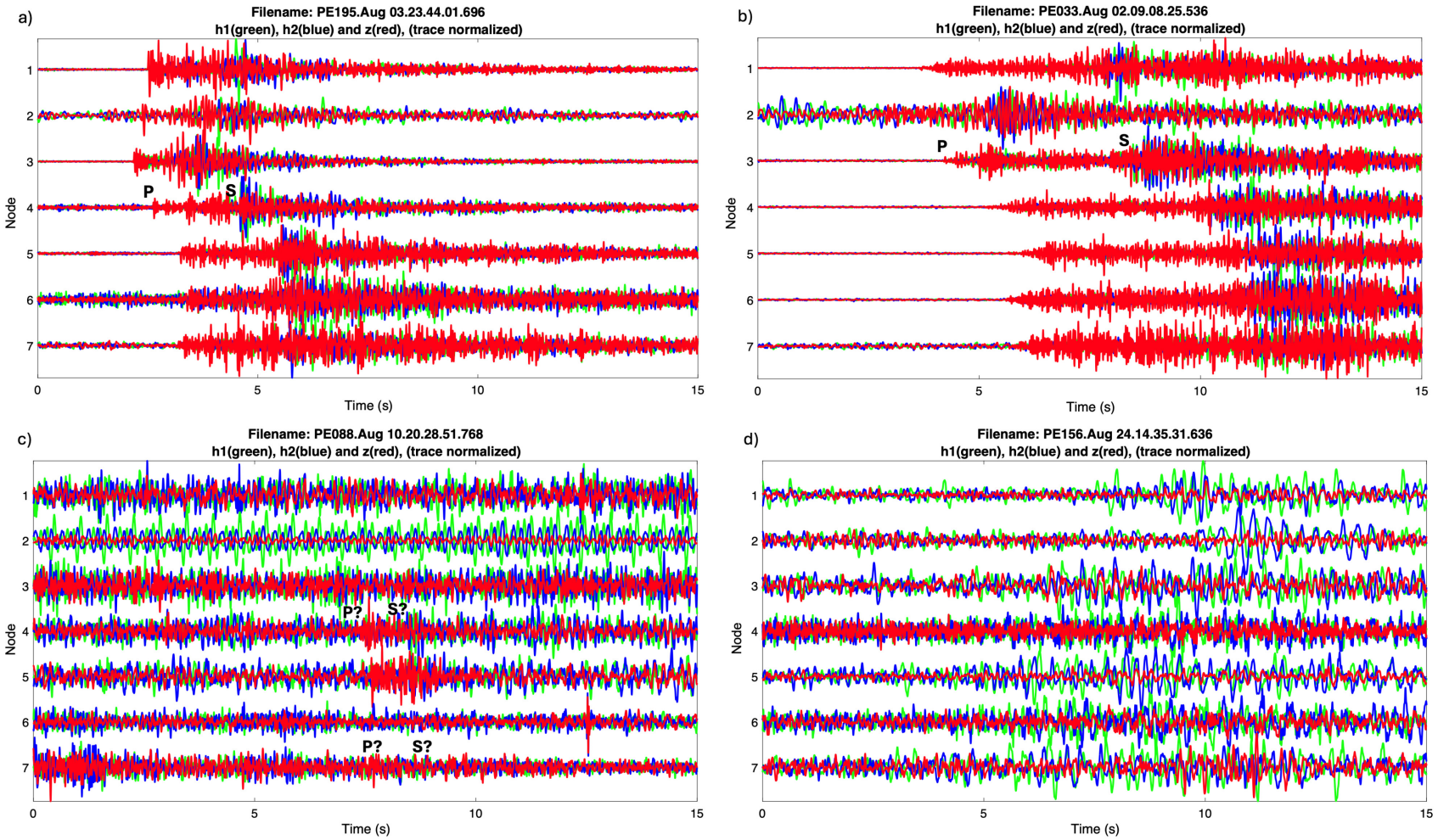

Figure 6. Seismograms of examples of excellent and probable events, and a noise record: (a) excellent event; (b) excellent event with a longer P-wave (P indicates arrival time) to S-wave (S indicates arrival time) travel-time distance; (c) probable event; (d) noise record. The data include two horizontal components, h1 (in green) and h2 (in blue), and a vertical component, z (in red).

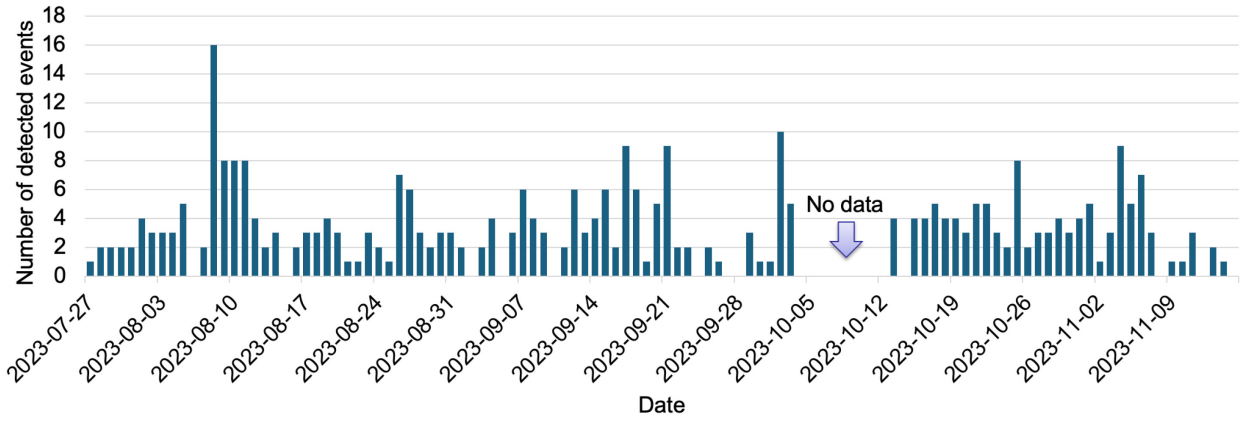

Figure 7. Events identified from three rounds of data by using the short-time average / long-time average method. Between October 5 and October 12, 2023, no nodal array data were available due to a gap before the third deployment of nodes; consequently, no events were recorded during this time.

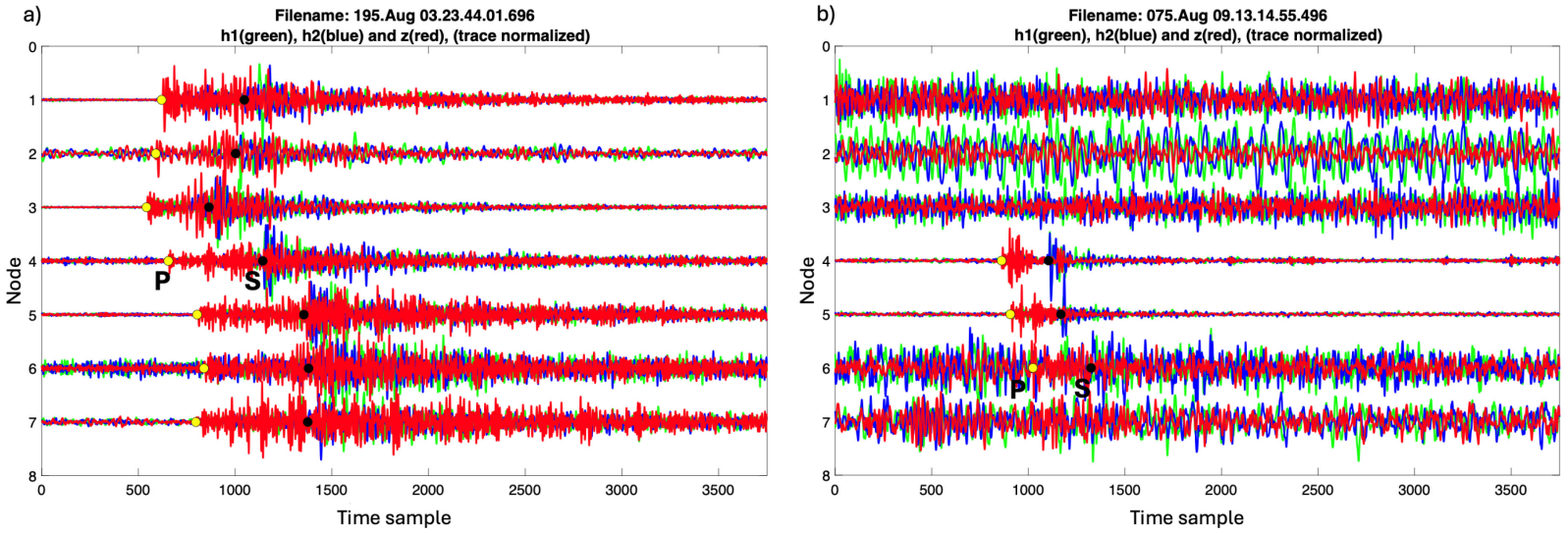

Figure 8. Examples of P-wave arrival picks (yellow dots) and S-wave arrival picks (black dots) on (a) a high-quality waveform and (b) a noisy waveform. The data include two horizontal components, h1 (in green) and h2 (in blue), and a vertical component, z (in red).

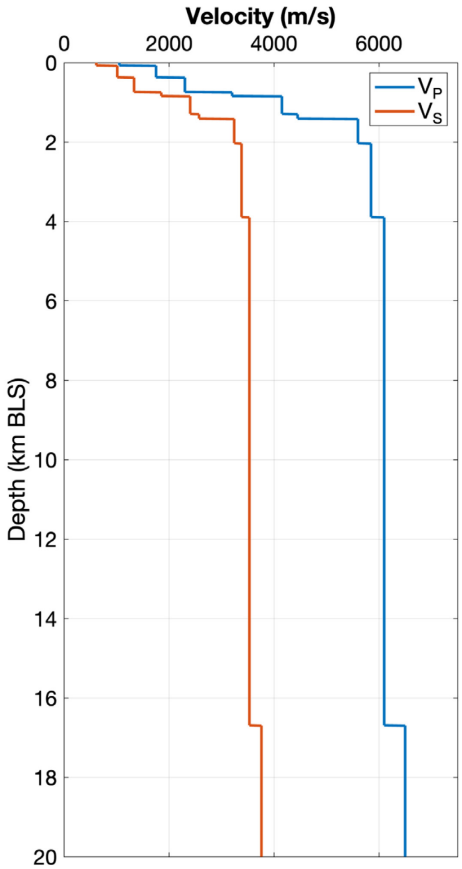

Figure 9. One-dimensional (1D) velocity model for the Peace River region, northwestern Alberta. Abbreviations: BLS, below land surface; V_P, P-wave velocity; V_S, S-wave velocity.

3.3 Event Location

Figure 9 shows the one-dimensional (1D) velocity model of P- and S-waves specifically designed for the Peace River region and used for locating seismic events in this area. The velocity model was constructed using sonic log measurements and geological top information for shallow depths, whereas the deeper part of the model was adapted from an AGS crustal velocity model.

Using P- and S-wave arrival time picks and the Peace River 1D velocity model, 340 events detected from the three rounds of nodal array data were located using the NonLinLoc software package (Lomax et al., 2000, 2014). The software has various options depending on event type (e.g., local or teleseismic), wave type, search space, velocity model (e.g., 1D or three dimensional [3D]), predicted travel-times calculation, search type (e.g., oct-tree, Metropolis-Gibbs), and location method.

This study focuses on local seismic events; therefore, NonLinLoc Non-Global mode was used for event location. The software includes a P-wave velocity / S-wave velocity (V_P/V_S) ratio setting that can be positive or negative, allowing for location based on either a single phase (e.g., P-waves) or both P- and S-waves. The V_P/V_S ratio was set to a negative value to include both P- and S-wave arrival times in the misfit calculation. For the search space, the program defines a 3D grid using coordinates of a user-defined origin, the number of grid points in x, y, and z directions, and grid spacing that includes the node locations.

Figure 10a–Figure 10c shows map and depth views of the locations of five large-magnitude events plotted along with node locations. To validate event locations obtained from the nodal array data, they were compared with event locations determined from the regional array. Event locations for both datasets were

determined using the same velocity model. From this comparison, strong similarities in event locations of the large-magnitude events were observed between the two arrays, providing confidence in the nodal array results.

Figure 11a–Figure 11c shows map and depth views of the locations of all events detected by the nodal array, plotted together with events detected by the regional array in the Peace River region. Overall, the event locations from the nodal array align well with the regional seismicity. Three main clusters are observed in the Peace River region from both the nodal and regional array data. The primary depth distribution of the nodal array events is between 4 and 6 km below the surface, suggesting the occurrence of events in the Precambrian basement. Additionally, a small cluster of 26 events near latitude 56.3°N, longitude 117°W, located within 15 km of disposal wells, was not detected by the regional array (Figure 11a). This highlights the improved local resolution of seismic event locations achieved using the nodal array data.

To quantify uncertainties in event locations, error ellipsoids derived from the covariance matrix of the probability density function (PDF) of the hypocentre locations were used. Figure 12a shows the 3D error ellipsoids, while the corresponding map and depth views are shown in Figure 12b–Figure 12d. These ellipsoids provide a compact and approximate representation of spatial uncertainty in event location. The 68% confidence level indicates that, assuming a perfectly ellipsoidal PDF, there is a 68% probability that the true hypocentre lies within the ellipsoid.

Figure 12 shows that seismic events located closer to the nodal array exhibit smaller error ellipsoids, indicating lower uncertainty in hypocentre location compared to events farther east and southeast. These results are expected, as shorter event-to-node distances typically yield higher-quality seismic signal recordings. Events near the nodal array benefit from increased signal amplitude and clarity, which produce more reliable phase picks and more accurate event locations. In contrast, events located farther from the array often generate weaker signals due to energy attenuation and potential interference during wave propagation, resulting in noisier signals, which impacts the accuracy of the phase picks and thus reduces the location accuracy. Furthermore, as seismic waves propagate over longer distances, their travel paths are increasingly influenced by heterogeneities in the velocity model, such as variations in lithology, stratification, and fracturing. For nearby events, the shorter travel paths minimize the impact of velocity model errors on calculated travel times, thereby improving location precision.

It was observed that several events have estimated hypocentre depths located at or near the surface. This is likely due to uncertainties in the absolute event locations. Given the limited station coverage and uncertainties in the velocity model, these events likely have double PDFs, making it difficult for the algorithm to determine an optimal hypocentre location. Event location accuracy can be improved by applying relative location algorithms such as hypoDD (Waldhauser, 2001), which refines relative event locations by minimizing travel-time differences between event pairs recorded at common stations, helping reduce errors from local velocity model uncertainties and station effects.

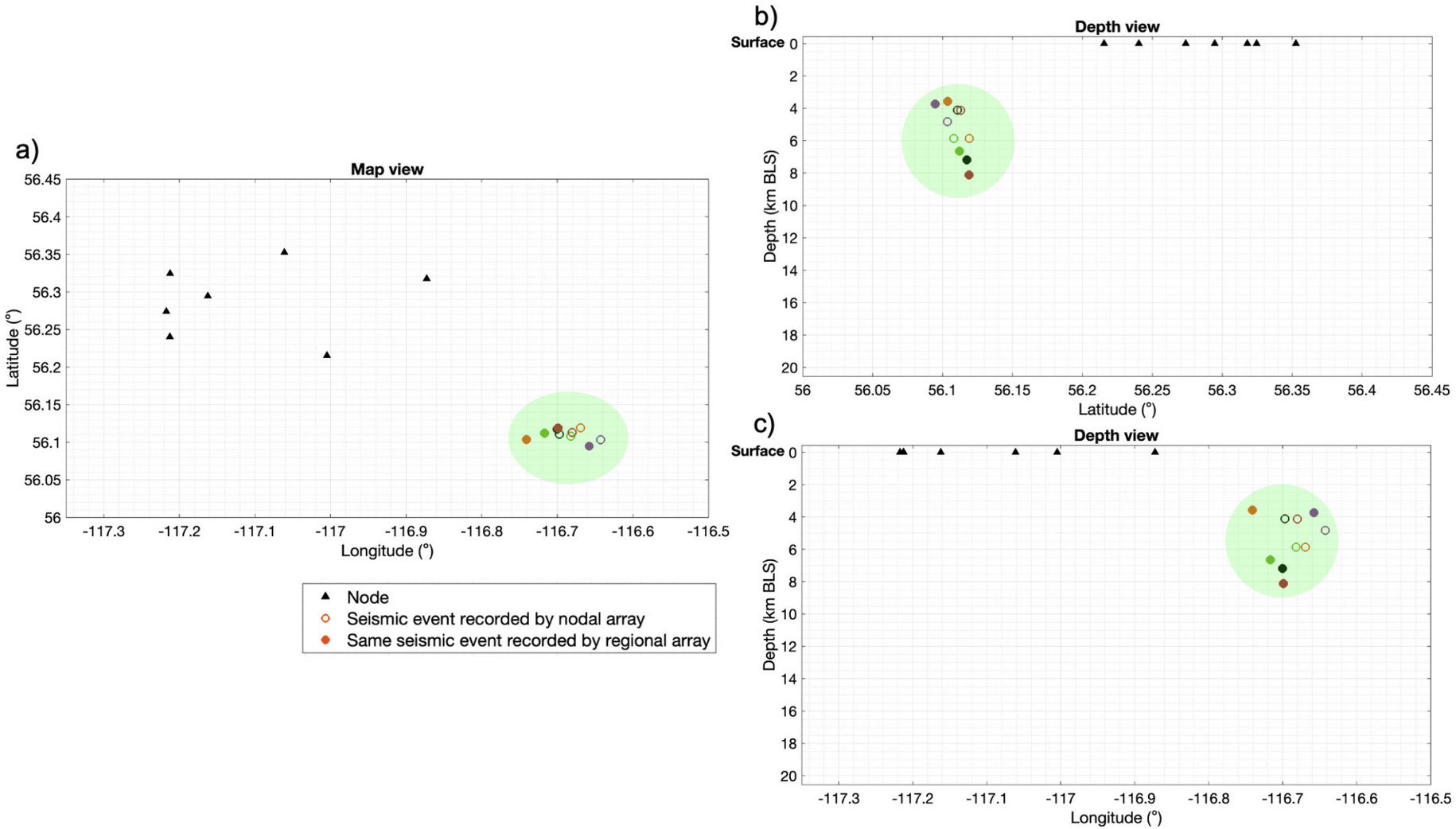

Figure 10. Comparison between seismic event locations obtained from the nodal array data and the locations of the same events (highlighted within the large filled green circle) detected by the regional seismic array (Alberta Geological Survey, 2026) in the Peace River region, northwestern Alberta, between July 27 and November 15, 2023: (a) map view; (b) and (c) depth views. All events were located using the Peace River one-dimensional velocity model (Bui et al., 2024). Abbreviation: BLS, below land surface.

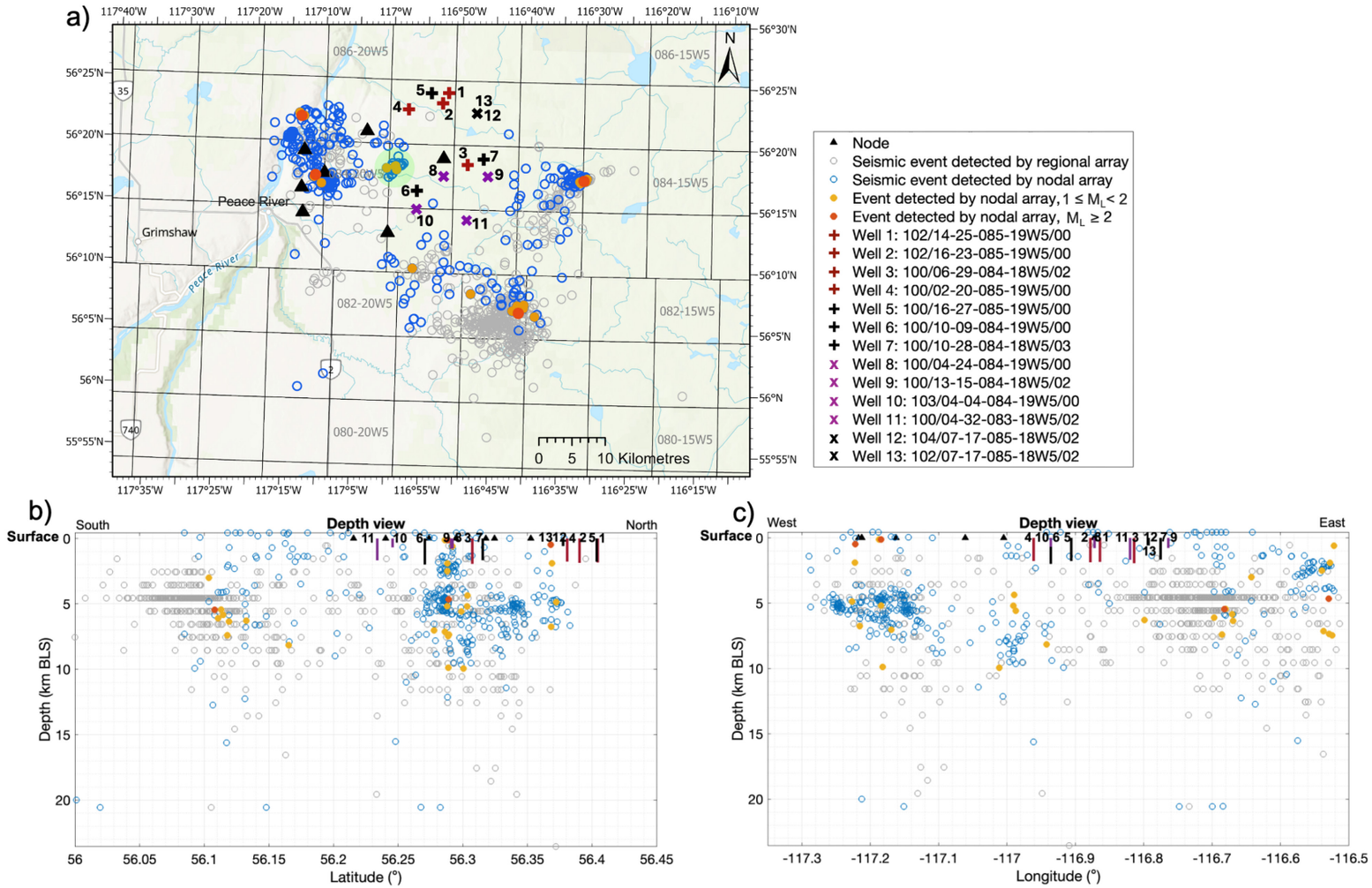

Figure 11. (a) Map and (b) and (c) depth views of 340 seismic events detected and located using nodal array data (open blue circles; July 27 to November 15, 2023), plotted together with node locations (black triangles), nearby disposal wells (labelled with numbers), and background seismicity from the regional array (open gray circles; January 2009 to February 2026; Alberta Geological Survey, 2026) in the Peace River region, northwestern Alberta. Filled green circle indicates area with 26 events not detected by the regional array. Abbreviations: BLS, below land surface; M_L, local magnitude.

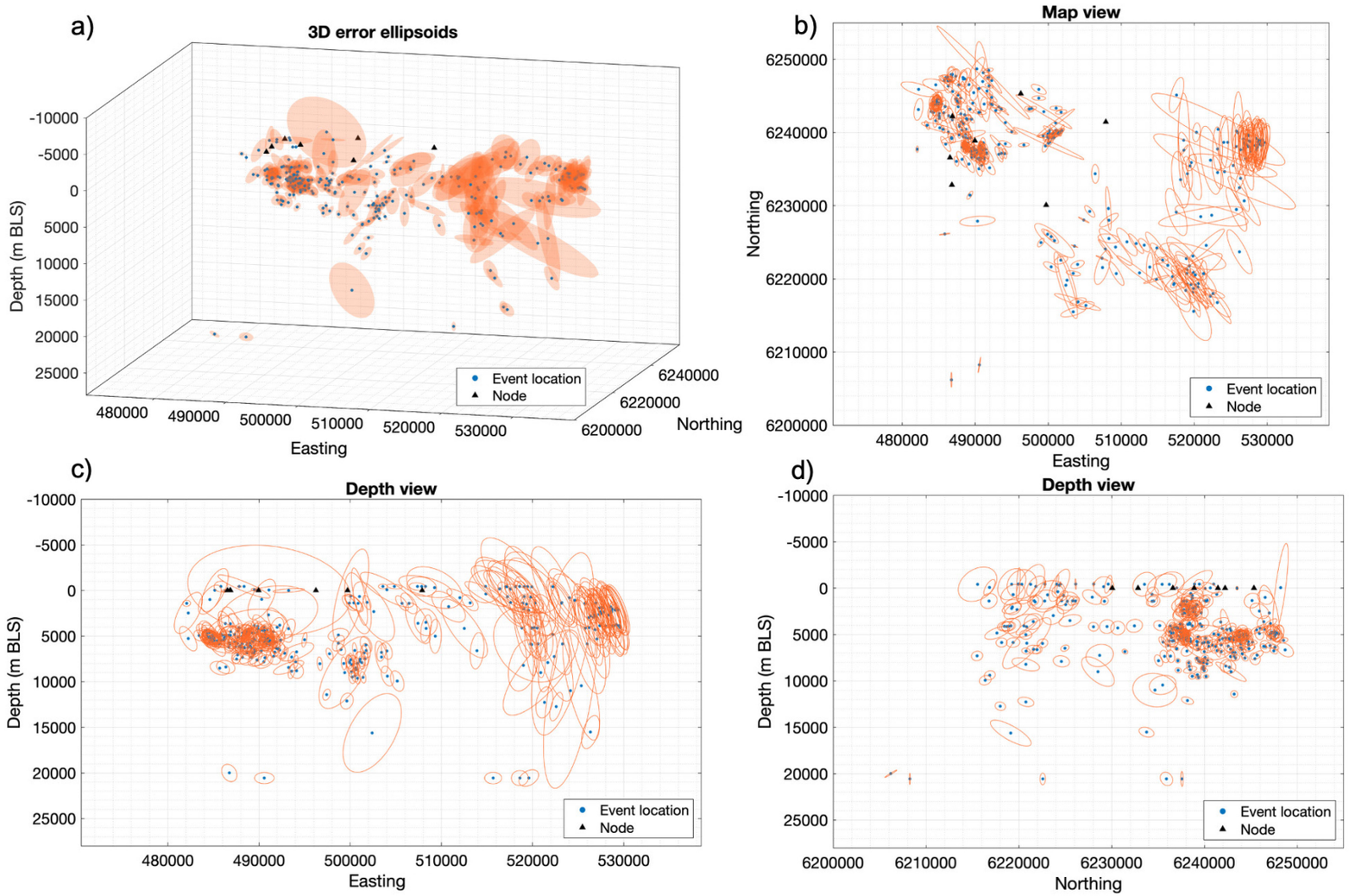

Figure 12. Estimated error in seismic event locations (error ellipsoids) in the Peace River region, northwestern Alberta, July 27 to November 15, 2023: (a) three-dimensional (3D) error ellipsoids; (b) map view; (c) and (d) depth views. Node locations and event locations are indicated by black triangles and blue circles, respectively. All coordinates are in UTM Zone 11N, NAD83. Abbreviation: BLS, below land surface.

3.4 Local Magnitude Calculation and Catalogue Building

Figure 13 shows the histogram of local magnitudes for 340 events detected from the three rounds of nodal array data, calculated using the equations by Yenier (2017; Equations 9 and 10).

The magnitude of completeness (Mc), estimated using the maximum curvature method (MCM; Wiemer and Wyss, 1997), is approximately 0, indicating that all earthquakes above this threshold are considered to be reliably detected and recorded. Considering the error from MCM, the Mc should not be higher than 0.1.

Applying the maximum likelihood method (MLM; Aki, 1965) to the nodal array catalogue with Mc = 0 yields Gutenberg-Richter parameters of b = 0.77 ±0.04 and a = 2.9894, with negligible error in the a value due to Mc = 0. The frequency-magnitude distribution above Mc follows the expected exponential decay, consistent with the Gutenberg-Richter (GR) law, and the largest recorded local magnitude is M_L = 2.83.

The local magnitude estimation results of the seismic nodal array data were compared with the magnitude of events detected by the regional array. Table 1 shows the comparison results of 12 events with M_L ≥1.5 detected by both arrays. Overall, similar magnitudes were obtained for the same events, albeit slightly higher results for events in the North Peace River cluster from the nodal array data (highlighted in bold in the table), which is expected as the local array is closer to the event epicentres. The regional array missed two events, M_L = 1.70 and 1.65.

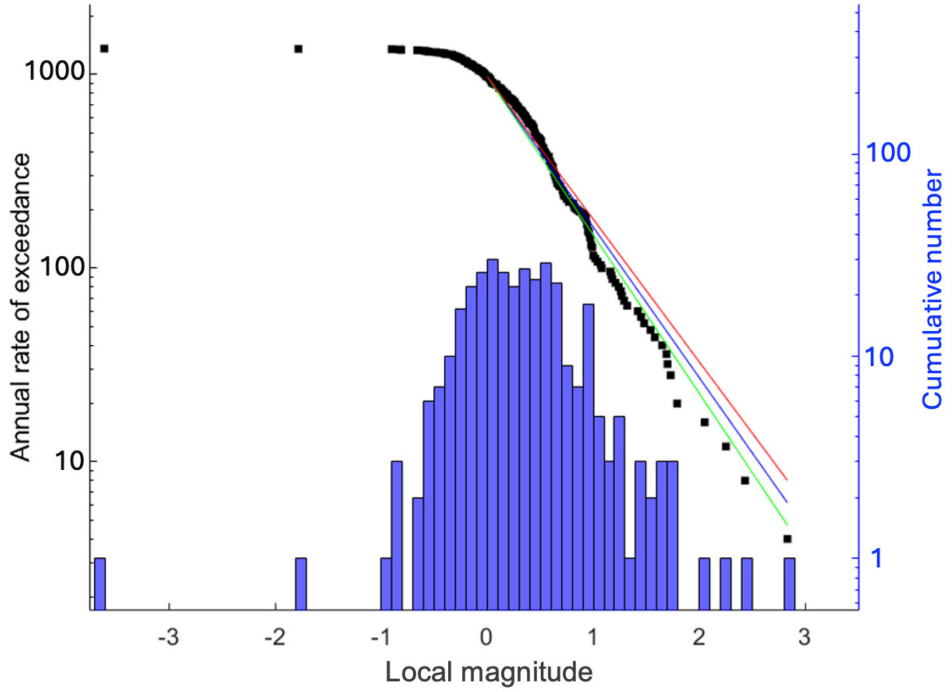

Figure 13. Histogram of local magnitude estimates for seismic events recorded by the nodal array in the Peace River region, northwestern Alberta, between July 27 and November 15, 2023. Black squares represent the observed annual rate of exceedance for each magnitude bin, plotted on a logarithmic scale. The central blue line shows the Gutenberg-Richter (GR) parameters estimation, using the maximum likelihood method (Aki, 1965). The upper (red) and lower (green) curves show the uncertainty bounds of the GR parameters estimation.

3.5 Source Mechanism Analysis

The Peace River region contains a complex network of faults (Gu et al., 2025). To further understand the source mechanisms of seismic events in the study area, events with $M_L \geq 1.5$ were selected (Table 1) and a moment tensor analysis was performed using amplitudes of P- and S-waves from all three data components. Details on the workflow and case studies of moment tensor inversion using amplitude data are described in Bui et al. (2024).

Figure 14 shows the moment tensor solutions for 11 seismic events (events 1–10 and 12 in Table 1; the result for event 11 was excluded after careful inspection of the inversion outputs). These solutions are displayed as beachball plots, overlaid on a topographic map that highlights major tectonic features, including the Peace River–Athabasca Arch and the eastern boundary of the Buffalo High–Utikuma High domain of the Precambrian basement (Alberta Geological Survey, 2021), as well as lineaments interpreted from petroleum well log data and structural residual surfaces, covering the Cretaceous to Precambrian interval (Mei, 2006). The seismic event locations obtained from the nodal array data are also plotted on this map for reference. The moment tensor inversion of the selected seismic events shows that the majority of these events exhibit reverse faulting mechanisms. The fault strikes appear to be aligned with pre-existing lineaments identified in available data from the Peace River region (Mei, 2006).

4 Discussion

The processing of seismic nodal array data is essential for the detection of seismic events and for improving the understanding of seismic clusters and their origin. In this report, a complete processing workflow capable of processing hundreds of gigabytes of data is described and applied to the North Peace River earthquake sequence. The processing workflow provided a high-quality earthquake catalogue with event locations and local magnitudes of some of the largest events, which were comparable to the results obtained from the regional array data.

Table 1. List of 12 events with local magnitude (M_L) ≥1.5 detected by the seismic nodal array during the three rounds of deployment (July 27 to November 15, 2023), Peace River region, northwestern Alberta. The table includes a comparison to the M_L of the same events detected by the regional array (Alberta Geological Survey, 2026). Abbreviations: dd, day; HH, hour; mm, month; MM, minute; SS, second; yyyy, year.

Event Number	Event Date (yyyy-mm-dd)	Event Time (HH:MM:SS)	M_L from Nodal Array Data	M_L from Regional Array Data
1	**2023-08-08**	**03:09:16.421**	**2.25**	**1.95**
2	2023-08-16	05:19:29.489	1.58	1.86
3	2023-08-20	02:04:23.489	1.79	1.79
4	2023-09-04	20:30:05.904	1.73	1.97
5	**2023-09-12**	**22:46:34.421**	**2.43**	**1.65**
6	**2023-09-15**	**12:01:35.794**	**1.73**	**1.42**
7	**2023-09-20**	**19:34:35.618**	**1.70**	**Missed**
8	**2023-09-21**	**15:57:05.775**	**1.65**	**Missed**
9	2023-10-02	10:20:36.596	2.05	2.44
10	2023-10-02	10:25:27.103	1.54	1.82
11	**2023-10-29**	**02:05:33.525**	**1.69**	**1.24**
12	2023-11-04	07:23:40.257	2.83	2.83

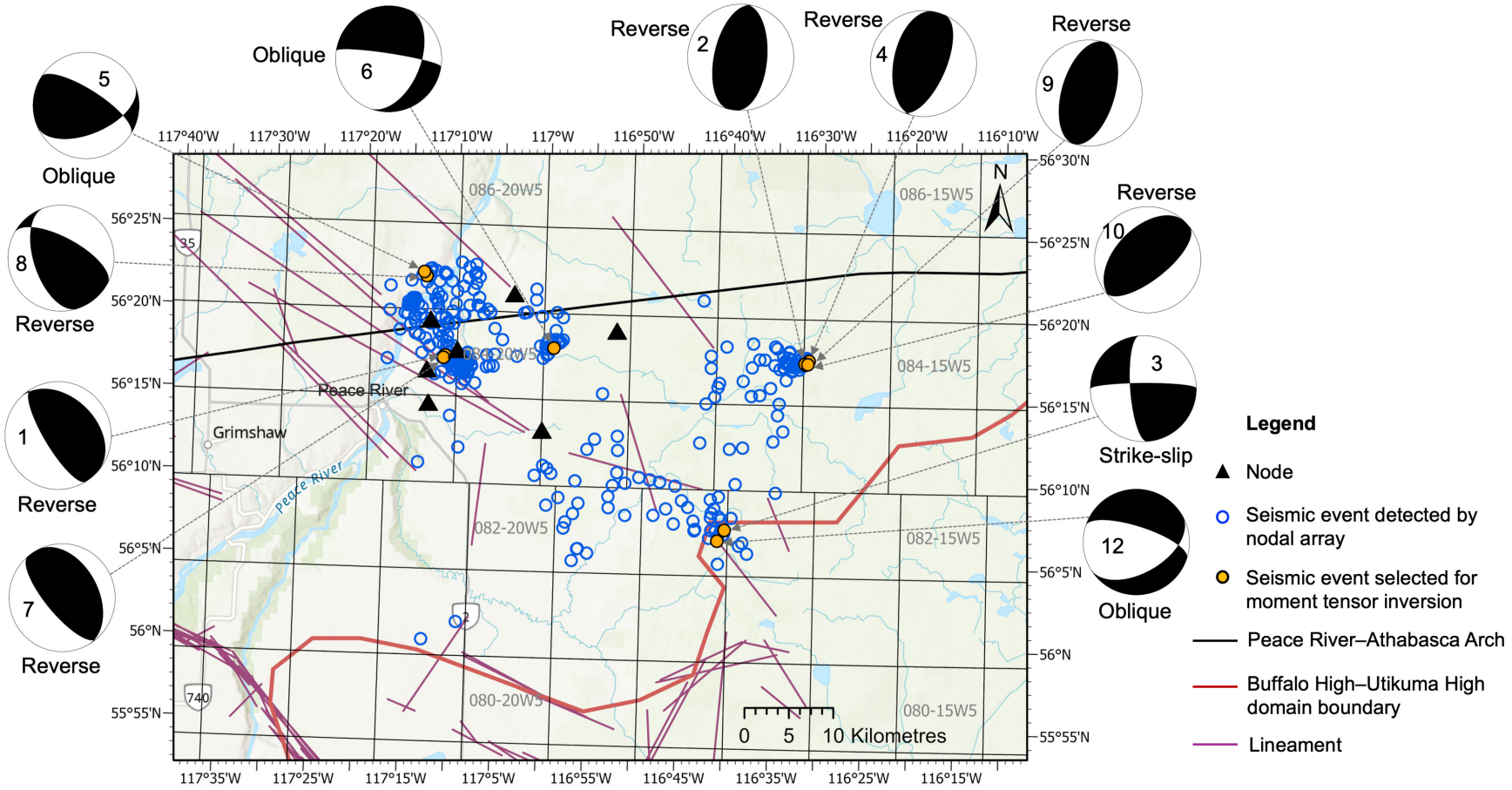

Figure 14. Moment tensor inversion of selected seismic events (orange circles; see associated event numbers in Table 1 for further information) in the Peace River region, northwestern Alberta. All of the seismic event locations (blue circles) obtained from the nodal array data (July 27 to November 15, 2023) are also plotted on this map for reference. Major tectonic features (Peace River–Athabasca Arch and Buffalo High–Utikuma High domain boundary; Alberta Geological Survey, 2021) and lineaments (covering the Cretaceous to Precambrian interval; Mei, 2006) are also shown.

There are several ways to improve the performance of the processing workflow, especially where there are alternative and more refined approaches that can be employed. For example, the use of an STA/LTA energy-based detector produces a large number of false alarms, and manual review of these results can take a long time. This issue can be addressed by exploring more efficient detection methods, such as time-frequency-based detectors like the well-known PhaseNet (Zhu and Beroza, 2019) and the recently developed Cluster Analysis of Trimmed Spectrograms (CATS; Grubas and van der Baan, 2025). Some preliminary testing results were obtained for a partial section of the nodal array dataset using CATS, and they showed that CATS significantly reduces false positives compared to the STA/LTA method, thus decreasing the time required for manual inspection and classification. However, further testing is necessary before applying this method to the entire nodal array dataset.

Interpretation of source mechanisms from selected events in the North Peace River seismic cluster provides additional insight into the complex fault networks of the region. However, initial analysis shows that the fault systems in the Peace River region are very intricate, which is to be expected from an area with complex tectonism.

Current work is planned to fully determine the origin of the seismicity in the North Peace River earthquake sequence, including the application of evidence-based scoring tools (Reyes Canales et al., 2026) to help discern the natural versus induced origin of the earthquake sequence.

5 Conclusions

This report provides a comprehensive workflow for processing seismic nodal array data, including preprocessing, potential event detection, seismic phase picking, event location, local magnitude estimation, catalogue building, and moment tensor inversion. Each step is described in detail, outlining the methods used and their application to raw data collected from the area north of the town of Peace River.

The use of a nodal array offers significant benefits for rapid and cost-effective deployment and provides high-resolution analysis of local seismicity. The improved location accuracy provided by the nodal array can support a better understanding of the causes (natural or induced) of seismic clusters. Nodal arrays also enable detection of events that may be missed by regional networks, offering valuable insight into the evolution of earthquake sequences. Application of the processing workflow to three rounds of nodal array data collected in the area north of the town of Peace River shows that with just three months of deployment, the nodal array detected 340 seismic events in the Peace River region, with the largest event in the catalogue having a local magnitude of 2.83. Among these, 29 events have local magnitudes greater than or equal to 1, and 13 of these events were not detected by the regional array. Despite the limited spatial coverage with only seven nodes, the event locations show strong agreement with those recorded by the regional array. Most events occurred at depths between 4 and 6 km below the surface, suggesting the occurrence of events in the Precambrian basement. The nodal array detected a small cluster of 26 events within a 15 km radius of disposal wells that was not previously observed in the regional data. These pieces of evidence are key in the current assessment aimed at understanding the origin of this earthquake sequence.

There are several ways to improve the efficiency and accuracy of the processing workflow for nodal array data. One approach is to employ more efficient detection methods, such as machine-learning-based techniques, to minimize the time required for manual event inspection and classification. Event relocation using the hypoDD method can also be applied to improve location accuracy; however, careful testing is necessary to validate the results.

6 References

Aki, K. (1965): Maximum likelihood estimate of b in the formula logN = a − bM and its confidence limits; Bulletin of the Earthquake Research Institute, v. 43, p. 237–239.

Aki, K. and Richards, P.G. (2002): Quantitative seismology (2nd edition); University Science Books, Meville, New York, 700 p.

Akram, J. and Eaton, D.W. (2016): A review and appraisal of arrival-time picking methods for downhole microseismic data; Geophysics, v. 81, no. 2, p. KS71–KS91.

Alberta Energy Regulator (2026): Directive 065: Resources applications for oil and gas reservoirs; Alberta Energy Regulator, URL < https://static.aer.ca/prd/documents/directives/Directive065.pdf> [March 2026].

Alberta Energy Regulator (2025): How to submit seismic waveform data; Alberta Energy Regulator, URL <https://static.aer.ca/prd/documents/manuals/Manual-032.pdf> [March 2026].

Alberta Energy Regulator (2024): Subsurface Order No. 2A; Alberta Energy Regulator, URL <https://static.aer.ca/prd/documents/orders/subsurface-orders/so2a.pdf> [February 2026].

Alberta Energy Regulator (2019): Subsurface Order No. 7; Alberta Energy Regulator, URL <https://static.aer.ca/prd/documents/orders/subsurface-orders/SO7.pdf> [August 2025].

Alberta Geological Survey (2021): Selected tectonic features; Alberta Energy Regulator / Alberta Geological Survey, URL <https://geology-ags-aer.opendata.arcgis.com/datasets/ags-aer::selected-tectonic-features/about> [December 2025].

Alberta Geological Survey (2026): Alberta Earthquake Dashboard; Alberta Energy Regulator / Alberta Geological Survey, URL <https://ags-aer.shinyapps.io/Seismicity_waveform_app/> [February 2026].

Allen, R.V. (1978): Automatic earthquake recognition and timing from single traces; Bulletin of the Seismological Society of America, v. 68, no. 5, p. 1521–1532.

Berg, M.E. (2022): A geophysicist's guide to the Fairfield nodes; Sandia National Laboratories, No. SAND2022-3701, 77 p.

Boore, D.M. (1989): The Richter scale: its development and use for determining earthquake source parameters; Tectonophysics, v. 166, no. 1–3, p. 1–14.

Bormann, P., Engdahl, B. and Kind, R. (2012): Seismic wave propagation and Earth models; *in* New manual of seismological observatory practice 2 (NMSOP2), P. Bormann (ed.), Deutsches GeoForschungsZentrum GFZ, Potsdam, Germany, p. 1–105.

Bui, H. and van der Baan, M. (2020): Event detection using a fast matched filter algorithm - an efficient way to deal with big microseismic data sets; Society for Exploration Geologists, 90th Annual International Meeting, Virtual, October 11–16, 2020, SEG Technical Program Expanded Abstracts, p. 1325–1329.

Bui, H. and van der Baan, M. (2024): Event locations: speeding up grid searches using quadratic interpolation; Geophysical Journal International, v. 239, no. 3, p. 1799–1820.

Bui, H., Stern, V.H., Yusifbayov, J.A., Reyes Canales, M. and Roman, N.L. (2024): Moment tensor analysis for the local magnitude 3.7 seismic event on June 25, 2022, near Hinton, central Alberta; Alberta Energy Regulator / Alberta Geological Survey, AER/AGS Open File Report 2024-02, 27 p.

Castellanos, F. and van der Baan, M. (2015): Waveform similarity for quality control of event locations, time picking, and moment tensor solutions; Geophysics, v. 80, no. 6, p. WC99–WC106.

Cipolla, C., Maxwell, S., Mack, M. and Downie, R. (2011): A practical guide to interpreting microseismic measurements; SPE North American Unconventional Gas Conference and Exhibition, The Woodlands, Texas, June 14–16, 2011, paper no. SPE-144067–MS.

Eaton, D.W. (2018): Passive seismic monitoring of induced seismicity: fundamental principles and application to energy technologies; Cambridge University Press, Cambridge, United Kingdom.

Eisner, L., Duncan, P.M., Heigl, W.M. and Keller, W.R. (2009): Uncertainties in passive seismic monitoring; Leading Edge, v. 28, no. 6, p. 648–655.

Eisner, L., Hulsey, B., Duncan, P., Jurick, D., Werner, H. and Keller, W. (2010): Comparison of surface and borehole locations of induced seismicity; Geophysical Prospecting, v. 58, no. 5, p. 809–820.

Eyre, T.S. and van der Baan, M. (2015): Overview of moment tensor inversion of microseismic events; The Leading Edge, v. 34, no. 8, p. 882–888.

Eyre, T.S. and van der Baan, M. (2017): The reliability of microseismic moment-tensor solutions: surface versus borehole monitoring; Geophysics, v. 82, no. 6, p. KS113–KS125.

Forouhideh, F. and Eaton, D.W. (2009): Microseismic monitoring: insights from moment tensor inversion; CREWES Research Report, v. 21, 19 p.

Grubas, S. and van der Baan, M. (2025): Three-component denoising of earthquake signals with CATS-3C; Canadian Energy Geoscience Association–Canadian Society of Exploration Geophysicists, Joint Annual Meeting (GeoConvention 2025), Calgary, Alberta, May 12–14, 2025, abstract, 4 p., URL <https://geoconvention.com/wp-content/uploads/abstracts/2025/114466-three-component-denoising-of-earthquake> [August 2025].

Gu, Y.J., Sun, W., Yu, T.C., Wang, J., Wang, R., Li, T. and Schultz, R. (2025): Peace River induced seismic monitoring (PRISM) nodal seismic array; Seismological Research Letters, v. 96, no. 1, p. 562–575.

Gutenberg, B. and Richter, C.F. (1956): Earthquake magnitude, intensity, energy, and acceleration (second paper); Bulletin of the Seismological Society of America, v. 46, no. 2, p. 105–145.

Hansen, S.M. and Schmandt, B. (2015): Automated detection and location of microseismicity at Mount St. Helens with a large-N geophone array; Geophysical Research Letters, v. 42, no. 18, p. 7390–7397.

Hardebeck, J.L. and Shearer, P.M. (2003): Using S/P amplitude ratios to constrain the focal mechanisms of small earthquakes; Bulletin of the Seismological Society of America, v. 93, no. 6, p. 2434–2444.

Havskov, J. and Ottemoller, L. (2010): Routine data processing in earthquake seismology: with sample data, exercises and software; Springer, Dordrecht, Netherlands, 347 p.

Li, J., Rojas-Parra, J., Salvage, R.O., Eaton, D.W., Innanen, K.A., Gu, Y.J. and Sun, W. (2024): Machine learning aids rapid assessment of aftershocks: application to the 2022–2023 Peace River earthquake sequence, Alberta, Canada; The Seismic Record, v. 4, no. 1, p. 21–31.

Li, T., Gu, Y.J., Wang, J., Wang, R., Yusifbayov, J., Reyes Canales, M. and Shipman, T. (2022): Earthquakes induced by wastewater disposal near Musreau Lake, Alberta, 2018–2020; Seismological Research Letters, v. 93, no. 2A, p. 727–738.

Lomax, A. and Curtis, A. (2001): Fast, probabilistic earthquake location in 3D models using Oct-Tree importance sampling; Geophysical Research Abstracts, v. 3, p. 955.

Lomax, A., Michelini, A. and Curtis, A. (2009): Earthquake location, direct, global-search methods; *in* Encyclopedia of complexity and systems science, R.A. Meyers (ed.), Springer, New York, New York, p. 2449–2473.

Lomax, A., Michelini, A. and Curtis, A. (2014): Earthquake location, direct, global-search methods; *in* Encyclopedia of complexity and systems science, R.A. Meyers (ed.), Springer, New York, New York, p. 1–33, doi:10.1007/978-3-642-27737-5_150-2.

Lomax, A., Virieux, J., Volant, P. and Berge-Thierry, C. (2000): Probabilistic earthquake location in 3D and layered models: introduction of a Metropolis-Gibbs method and comparison with linear locations; *in* Advances in seismic event location, C.H. Thurber and N. Rabinowitz (ed.), Modern Approaches in Geophysics, v. 18, Springer, Dordrecht, Netherlands, p. 101–134.

Maxwell, S.C. (2014): Microseismic imaging of hydraulic fracturing: improved engineering of unconventional shale reservoirs; Society of Exploration Geophysicists, Distinguished Instructor Series, No. 17, 197 p.

Mei, S. (2006): Structures and faults in the Peace River Arch Region, Alberta, 2006 (GIS data, line features); Alberta Energy and Utilities Board, EUB/AGS, URL <https://ags.aer.ca/publications/all-publications/dig-2007-0011> [December 2025].

Mesimeri, M., Pankow, K.L. and Rutledge, J. (2021): A frequency-domain-based algorithm for detecting microseismicity using dense surface seismic arrays; Bulletin of the Seismological Society of America, v. 111, no. 5, p. 2814–2824.

Oye, V. and Roth, M. (2003): Automated seismic event location for hydrocarbon reservoirs; Computers & Geosciences, v. 29, no. 7, p. 851–863.

Pavlis, G.L. (1986): Appraising earthquake hypocenter location errors: a complete, practical approach for single-event locations; Bulletin of the Seismological Society of America, v. 76, no. 6, p. 1699–1717.

Reyes Canales, M., Hauck, T.E., Yusifbayov, J.A., Bui, H. and Goerzen, C. (2026): Discerning between natural and induced seismicity by using evidence-scoring tools designed to evaluate proposals of induced earthquakes: application to the Reno and Kakwa earthquake sequences, northwestern Alberta; Alberta Energy Regulator / Alberta Geological Survey, AER/AGS Open File Report 2025-05, 29 p.

Reyes Canales, M., Rodriguez-Pradilla, G., Yusifbayov, J. and van der Baan, M. (2022a): The rise, peak and decline of the seismic hazard related to hydraulic fracturing activities in the Duvernay play, Fox Creek area, Alberta; Journal of Geophysical Research: Solid Earth, v. 127, no. 1, doi: https://doi.org/10.1029/2021JB023060.

Reyes Canales, M., Yusifbayov, J. and van der Baan, M. (2022b): Evolution of short-term seismic hazard in Alberta, Canada, from induced and natural earthquakes: 2011–2020; Journal of Geophysical Research: Solid Earth, v. 127, no. 2, doi: https://doi.org/10.1029/2021JB022822 .

Ringler, A.T., Anthony, R.E., Karplus, M.S., Holland, A.A. and Wilson, D.C. (2018): Laboratory tests of three Z-Land Fairfield nodal 5-Hz, three-component sensors; Seismological Research Letters, v. 89, no. 5, p. 1601–1608.

Salvage, R.O., Eaton, D.W., Furlong, C.M., Dettmer, J. and Pedersen, P.K. (2024): Induced or natural? toward rapid expert assessment, with application to the Mw 5.2 Peace River earthquake sequence; Seismological Research Letters, v. 95, no. 2A, p. 758–772.

Schultz, R. and Stern, V. (2015): The regional Alberta observatory for earthquake studies network (RAVEN); CSEG Recorder, v. 40, no. 8, p. 34–37.

Schultz, R. and Wang, R. (2020): Newly emerging cases of hydraulic fracturing induced seismicity in the Duvernay East Shale Basin; Tectonophysics, v. 779, art. 228393.

Schultz, R., Stern, V., Novakovic, M., Atkinson, G. and Gu, Y.J. (2015): Hydraulic fracturing and the Crooked Lake sequences: insights gleaned from regional seismic networks; Geophysical Research Letters, v. 42, no. 8, p. 2750–2758.

Schultz, R., Wang, R., Gu, Y.J., Haug, K. and Atkinson, G. (2017): A seismological overview of the induced earthquakes in the Duvernay play near Fox Creek, Alberta; Journal of Geophysical Research: Solid Earth, v. 122, no. 1, p. 492–505.

Schultz, R., Woo, J.U., Pepin, K., Ellsworth, W.L., Zebkar, H., Segall, P., Gu, Y.J. and Samsonov, S. (2023): Disposal from in situ bitumen recovery induced the M_L 5.6 Peace River earthquake; Geophysical Research Letters, v. 50, no. 6, doi: https://doi.org/10.1029/2023GL102940.

Schultz, R.J., Yusifbayov, J. and Shipman, T.C. (2020): The Scientific Induced Seismicity Monitoring Network (SCISMN); Alberta Energy Regulator / Alberta Geological Survey, AER/AGS Open File Report 2019-09, 10 p.

Shearer, P.M., Meng, H. and Fan, W. (2023): Earthquake detection using a nodal array on the San Jacinto fault in California: evidence for high foreshock rates preceding many events; Journal of Geophysical Research: Solid Earth, v. 128, no. 3, doi: https://doi.org/10.1029/2022JB025279 .

Sheng, Y., Kong, Q. and Beroza, G.C. (2021): Network analysis of earthquake ground motion spatial correlation: a case study with the San Jacinto seismic nodal array; Geophysical Journal International, v. 225, no. 3, p. 1704–1713.

Sleeman, R. and Van Eck, T. (1999): Robust automatic P-phase picking: an on-line implementation in the analysis of broadband seismogram recordings; Physics of the Earth and Planetary Interiors, v. 113, no. 1–4, p. 265–275.

Stein, S. and Wysession, M. (2009): An introduction to seismology, earthquakes, and earth structure; John Wiley & Sons, 512 p.

Trnkoczy, A. (1999): Understanding and parameter setting of STA/LTA trigger algorithm; *in* New manual of seismological observatory practice 2 (NMSOP-2), P. Bormann (ed.), Deutsches GeoForschungsZentrum GFZ, Potsdam, Germany, p. 1–20.

Tsvankin, I., Gaiser, J., Grechka, V., van der Baan, M. and Thomsen, L. (2010): Seismic anisotropy in exploration and reservoir characterization: an overview; Geophysics, v. 75, no. 5, p. 75A15–75A29.

Waldhauser, F. (2001): hypoDD: a computer program to compute double-difference hypocenter locations; U.S. Geological Survey, Open-File Report 01–113, 25 p.

Waldhauser, F. and Ellsworth, W.L. (2000): A double-difference earthquake location algorithm: method and application to the Northern Hayward fault, California; Bulletin of the Seismological Society of America, v. 90, no. 6, p. 1353–1368.

Wang, J., Li, T., Gu, Y.J., Schultz, R., Yusifbayov, J. and Zhang, M. (2020): Sequential fault reactivation and secondary triggering in the March 2019 Red Deer induced earthquake swarm; Geophysical Research Letters, v. 47, no. 22, doi: https://doi.org/10.1029/2020GL090219 .

Wang, R., Gu, Y.J., Schultz, R., Kim, A. and Atkinson, G. (2016): Source analysis of a potential hydraulic-fracturing-induced earthquake near Fox Creek, Alberta; Geophysical Research Letters, v. 43, no. 2, p. 564–573.

Wiemer, S. and Wyss, M. (1997): Mapping the frequency-magnitude distribution in asperities: an improved technique to calculate recurrence times?; Journal of Geophysical Research: Solid Earth, v. 102, p. 15115–15128.

Withers, M., Aster, R., Young, C., Beiriger, J., Harris, M., Moore, S. and Trujillo, J. (1998): A comparison of select trigger algorithms for automated global seismic phase and event detection; Bulletin of the Seismological Society of America, v. 88, no. 1, p. 95–106.

Wuestefeld, A., Greve, S.M., Näsholm, S.P. and Oye, V. (2018): Benchmarking earthquake location algorithms: a synthetic comparison; Geophysics, v. 83, no. 4, p. KS35–KS47.

Yenier, E. (2017): A local magnitude relation for earthquakes in the Western Canada Sedimentary Basin; Bulletin of the Seismological Society of America, v. 107, no. 3, p. 1421–1431.

Yu, H., Kao, H., Visser, R. and Wang, B. (2021): From seismic quiescence to surged activity after decades of wastewater disposal: a case study in central-west Alberta, Canada; Geophysical Research Letters, v. 48, no. 22, doi: https://doi.org/10.1029/2021GL095074 .

Zhu, W. and Beroza, G.C. (2019): PhaseNet: a deep-neural-network-based seismic arrival-time picking method; Geophysical Journal International, v. 216, no. 1, p. 261–273.